THERMO ELASTIC STRESS ANALYSIS FOR DETECTION OF DAMAGE IN BEAMS

By

S M Arafath Uzzaman

Thesis
Submitted to Flinders University
for the degree of

Master of Engineering (Mechanical)

College of Science and Engineering
05.06.2024

TABLE OF CONTENTS

ABSTRACT

The effectiveness of thermoelastic stress analysis (TSA) for finding flaws in metal structural components is evaluated in this study. The study investigates the impact of varying loading conditions and defect locations on the efficacy of TSA in identifying damages. Experimental procedures involved cyclical bending loading to evaluate the effects of frequency and displacement on damage detectability. Additionally, a Finite Element model was developed to validate its accuracy under different load conditions and frequencies. The findings indicate that TSA is highly effective in precisely detecting and locating internal defects. Higher load amplitudes enhance detectability by reducing data noise, thus facilitating defect identification. In-plane amplitude measurements are particularly effective for detecting surface-level damages, while quadrature amplitude measurements excel in identifying defects by high peaks in the results section. Both high and low frequencies can identify damage locations; however, lower frequencies introduce noise into the results. There is a nonlinear link between TSA amplitude levels and frequency that needs further research. Although there is still need for further research on the implications of load signal frequency, the Finite Element model accurately covers a variety of cyclic bending loading scenarios. All things considered; this study validates TSA as a very effective full-field non-destructive testing technique for finding internal flaws in metals. Subsequent investigations need to look more into the nonlinear correlation between frequency and TSA amplitude levels, as well as expand on the potential of TSA.

DECLARATION

I certify that this thesis:

1. does not incorporate without acknowledgment any material previously submitted for a degree or diploma in any university
2. and the research within will not be submitted for any other future degree or diploma without the permission of Flinders University; and
3. to the best of my knowledge and belief, does not contain any material previously published or written by another person except where due reference is made in the text.

Signature of student: Sejan

Print name of student: S M Arafath Uzzaman

Date: 5th June 2024

I certify that I have read this thesis. In my opinion it is/is not (please circle) fully adequate, in scope and in quality, as a thesis for the degree of Master of Engineering (mechanical). Furthermore, I confirm that I have provided feedback on this thesis and the student has implemented it minimally/partially/fully (please circle).

Stuart Wildy Digitally signed by Stuart Wildy Date: 2024.06.06 07:37:24 +09'30'

Signature of Principal Supervisor: ....

Print name of Principal Supervisor: ...Dr Stuart Wildy..

Date: ...6/6/2024..

ACKNOWLEDGEMENTS

I would like to express my deep gratitude to all who have supported and guided me throughout the completion of this thesis. I am particularly thankful to my supervisor, Dr. Stuart Wildy, for his invaluable guidance and encouragement. His expertise and constructive feedback have been instrumental in shaping this research. Additionally, my heartfelt thanks go to my family for their unwavering love, belief in my abilities, and constant encouragement.

Finally, I would like to appreciate God for bestowing grace, mercy, encouragement, and unwavering assistance throughout my academic endeavours.

LIST OF FIGURES

LIST OF TABLES

CHAPTER ONE INTRODUCTION

Non-destructive testing (NDT) is the use of methods to assess the fatigue, fracture, structural integrity, surface flaws, or metallurgical condition of a material without causing harm or impacting its suitability for its intended use. (Dwivedi et al., 2018). This research assesses the effectiveness of Thermoelastic Stress Analysis (TSA) in detecting surface internal defects or damage in metal structural elements, exploring how different frequencies and displacement conditions and defect locations impact damage detectability.

Thermoelastic Stress Analysis (TSA) is an optical non-destructive testing (NDT) technique enabling the non-contact, full-field evaluation of surface stresses on objects. This method utilizes the thermoelastic effect, where cyclic stresses applied to a material cause temperature fluctuation. Under adiabatic conditions, these temperature changes in isotropic materials are directly proportional to the combined influence of the two principal stresses acting on the material's surface. (Gdoutos, 2022)

Structures are constructed from a variety of materials depending on their applications and uses. This thesis focuses exclusively on investigating defects and damage in mild steel to assess the precision of the TSA technique in detecting damages in metal beams. The evaluation of flaw detectability was conducted using two specific parameters: the frequency and amplitude of a steel beam's load under cyclical bending loading, and the location of damage in a steel beam under the same loading conditions.

Several advantages and disadvantages have been identified regarding the use of the TSA technique for damage detection. The most significant advantage is that it is a non-contact method, allowing for inspection without physical interaction. However, the efficacy of TSA decreases as the depth of the damage increases, resulting in less accurate detection at greater depths. Additionally, there is a paucity of research on how the depth at which IR cameras detect faults relative to the surface affects the TSA method's ability to identify internal metal damage

The TSA technique holds significant importance for several reasons. Firstly, as a non-destructive testing (NDT) method, it enables the assessment of material validity without causing damage. Secondly, TSA results clearly indicate areas requiring attention, which can help prevent catastrophic failures by addressing high-stress regions with extra care. Thirdly, the most crucial aspect of the TSA technique is its ability to detect damage locations. Identifying the origin of damage in large beams can be challenging, but TSA graphs and plots provide reliable documentation that pinpoint the exact locations of these damages

This research aims to assess the feasibility of using the TSA technique to detect surface and internal defects in metal structural elements by examining the effects of different frequencies, loading conditions, and defect locations. The first objective is to develop and implement an experimental protocol to evaluate how a steel beam's load amplitude and frequency under cyclical bending loading affect the detectability of damage using TSA. The second objective is to create a finite element model for the cyclical uniaxial loading experiment and evaluate its accuracy at different load amplitudes and frequencies. Lastly, the research involves analysing the data obtained from the test results.

The assumption was it can go through a good result and view the damage location and deep depth damages. Another thing was in phase amplitude was expected as considerable results of identifying peaks. However, quadrature amplitude measurements gave a better result.

Experiment is done under cyclic bending load with various frequencies level and obtained displacement as primary results and later going deep by observing amplitude, stress and temperature gradient or thermoelastic response signal. A FEA model is introduced to assess real experiment with simulation of different frequencies level. Different types of meshes are applied to evaluate the results. MATLAB is introduced to represents graphs and results to easy understanding.

This thesis begins by reviewing and assessing the relevant literature on the TSA technique to identify any gaps, aligning with the study's objectives and overall aim outlined in the Aim section. It then details the equipment used and develops the study methodology, incorporating the theoretical aspects of the TSA method. To aid the reader, the findings are presented clearly with graphical representations of the thermal response data. The thesis includes a critical analysis and discussion of the results, followed by a chapter that provides recommendations for future research and presents the conclusions.

CHAPTER TWO LITERATURE REVIEW

This literature review examines the use of Thermoelastic Stress Analysis (TSA) for the purpose of identifying deterioration in beams. The TSA methodology is a reliable method that uses the thermal characteristics of materials to identify hidden stress abnormalities. The technology of structural health monitoring is of great significance as it offers a non-invasive and very responsive method for finding flaws in beams. Furthermore, this research assesses the impact of several parameters, including as loading conditions and material properties, on the performance of TSA. Obtaining a thorough grasp of the current state of TSA in beam damage detection is essential for the further development and widespread use of this technology in structural engineering.

Methodology

Thermoelastic stress analysis (TSA) is a robust and non-destructive technique used to accurately measure stress and strain in materials and structures. Di Carolo et al. (2019) propose a unique approach that utilises thermoelectricity to investigate the relationship between elastic deformation and temperature. Thermoelastic Stress Analysis (TSA) is among the limited methods that provide full-field measurements of mechanical stress. Despite TSA systems being commercially available for over three decades and the introduction of rapid staring array systems nearly twenty years ago, the current utilization of TSA is not as extensive as initially expected by its early developers. (Ryall, T.G. and Wong, A.K., 1993) (Lesniak, J.R. and Boyce, B.R., 1994)

This objective serves as the main motivation for the current article, which outlines the development, validation, and application of a TSA system created with a compact, low-cost microbolometer device. The system, named MiTE, was initially reported in. (Rajic N, Weinberg S, Rowlands D.,2013)

Advanced processing methods are required to detect these discontinuities, as the raw thermal data is often insufficient. Popular infrared non-destructive testing (IRNDT) techniques include pulse thermography and lock-in thermography, used for various applications like coating thickness inspection. The microstructure and properties of thermal spray coatings are influenced by factors such as material type, spraying parameters, and environmental conditions. (Muzika, L., Švantner, M., Houdková, Š. and Šulcová, P., 2021)

With the increasing availability and affordability of thermocameras, thermography has transitioned from a rare technique to a popular investigation method. Military research initially advanced thermocamera technology for night vision, and its end of restrictions post-Cold War expanded civil applications. Classical thermography captures steady-state temperature differences, while dynamic techniques like lock-in thermography evaluate time-dependent temperature changes. Lock-in thermography introduces periodic heat to a sample, evaluating and averaging surface temperature modulations over time. This technique enhances sensitivity compared to pulse thermography and is crucial for detecting weak heat sources in electronic devices, improving failure analysis and testing. (Breitenstein, O. and Langenkamp, M., 2003.)

Flash pulse thermography involves short, intense heat pulses to inspect material properties and is quicker than lock-in thermography. It highlights differences in heat transfer, useful for detecting coating thickness variations, and requires calibration for accurate measurements. (Muzika, L., Švantner, M., Houdková, Š. and Šulcová, P., 2021)

Due to the sensitivity of fluorescent penetrant inspection to surface roughness, researchers have been exploring alternatives like vibrothermography, a contactless non-destructive testing method using high-frequency vibration pulses to create thermal gradients at defects. Thermographic cameras detect radiation within the 0.9-14 µm electromagnetic spectrum. Gülcan examined recent developments in vibrothermography, including its basics, history, equipment, materials, detection probability, heat generation mechanisms, and factors affecting detectability. (Gülcan, O., 2022.)

Thermal stress analysis holds significant importance across disciplines such as materials science, engineering, and physics, prompting researchers to employ diverse methodologies for its study. For instance, Chen et al. (2008) utilized an axisymmetric displacement-based thermo-elastic stress model to investigate thermal stresses during the solidification of a silicon ingot. Similarly, Xu et al. (2016) conducted thermal stress analysis to evaluate potential flaws in solid oxide fuel cell interconnects, while Lin (2024) showcased the application of APDL for automated construction and coupling analysis in a multichip module, aimed at comprehending its thermal behaviour.

Thermal stress analysis (TSA) stands out as an indispensable method for detecting damage in beams due to its sensitivity and ability to detect early-stage defects, such as microcracks or delamination, which might be missed by conventional techniques. Moreover, TSA offers the advantage of non-contact inspection, reducing the risk of additional stress or damage during examination, while providing real-time data crucial for continuous monitoring of structural integrity, especially under varying load cycles. Despite some limitations, such as the need for specialized equipment and restricted penetration depth, TSA's capability to analyze large beam constructions efficiently makes it a valuable tool in engineering and materials science research.

Limitation And Scope

Thermal stress analysis is subject to certain limits and challenges. Its reliance on the environment restricts it. The accuracy of thermal stress analysis measurements may be influenced by temperature and the thermal characteristics of the beam. Implementing TSA may be costly and complicated because to the need for precise equipment, such as high-speed infrared cameras and sophisticated data processing systems. Surface access is an additional concern. Due to its dependence on detecting surface heat and sensing, TSA is restricted to places that are easily accessible. As a result, its use is restricted to intricate or concealed structures. The TSA may have difficulties in identifying stress irregularities in materials that possess limited thermal conductivity. As a result of its high sensitivity, the method has the potential to provide inaccurate positive results, necessitating further examination. Thermoelastic Stress Analysis can identify beam damage because of its high sensitivity and capacity to detect faults in the early stages.

Finite element analysis has been widely used to quantify thermal stresses, as evidenced by Chawla et al. (2008) in their study on thermal stress in magnetron sputtered Ti coatings. Egilmez and Nalbant (2012) also applied finite element analysis to investigate thermal stresses in dental structures. Additionally, Sangwongwanich et al. (2020) explored reduced-order thermal modeling for photovoltaic inverters to assess long-term thermal stress.

Thermal stress analysis holds significant importance across disciplines such as materials science, engineering, and physics, prompting researchers to employ diverse methodologies for its study. For instance, Chen et al. (2008) utilized an axisymmetric displacement-based thermo-elastic stress model to investigate thermal stresses during the solidification of a silicon ingot. Similarly, Xu et al. (2016) conducted thermal stress analysis to evaluate potential flaws in solid oxide fuel cell interconnects, while Lin (2024) showcased the application of APDL for automated construction and coupling analysis in a multichip module, aimed at comprehending its thermal behaviour.

Area of agreement and disagreement

Thermal stress analysis can identify initial damage, such as microcracks or delamination, that may not be discovered by traditional methods due to its sensitivity to small stress variations. Since the TSA does not need direct contact with the item being examined, the likelihood of the examination causing extra stress or damage is reduced. It has the capability to provide data in real-time, allowing for ongoing monitoring of structural integrity while under stress. This is particularly useful for assessing fatigue-induced harm. The TSA is capable of effectively analysing large-scale beam structures due to its ability to include a substantial region in a single measurement.

The TSA sometimes requires specialised technology, such as costly high-speed infrared cameras and laser systems, which may need the presence of skilled operators. The major emphasis of this technique is mostly on the surface of the material, which may restrict its ability to detect flaws or damage that are located under the surface. External environmental variables, such as temperature and humidity, have the potential to impact the TSA, leading to inaccurate results in the form of false positives or negatives (Civera & Surace, 2022). TSA has a limited ability to penetrate deeply, making it useless for heavier beams or materials with complex interior structures.

Gap knowledge, Relevant gaps

TSA entails evaluating the effects of temperature fluctuations on materials, which induce cyclic thermal stress and can lead to the initiation of fatigue cracks (Hayashi & Hirano, 2012). Hayashi and Hirano research indicated that thermal fatigue cracks typically originate from specific points, such as carbides or notches, and propagate along grain boundaries or in particular directions under cyclic thermal stress (Zhang, 2023; Xia et al., 2011).

However, there is a lack of study on the impact of the depth at which IR camera-observed faults are located in relation to the surface on the TSA method's capacity to identify interior metal damage and also no one has looked at using TSA for subsurface detects in metal structures as well. No research has been done to assess the TSA technique's efficacy for metals with near-surface internal deterioration. There is a lack of extensive study data about the impact of different loading circumstances on the TSA method's capacity to identify internal metal damage.

Limitations of the research

Thermal stress analysis surpasses Ultrasonic Testing (UT) and Magnetic Particle Testing (MPT) in terms of its sensitivity and ability to monitor in real-time. For example, UT (ultrasonic testing) may detect faults inside an object, but it may not detect any damage on the surface. Nevertheless, Magnetic Particle Testing (MPT) is effective when used on ferrous materials but exhibits reduced performance when used to non-magnetic metals (Civera & Surace, 2022). TSA offers notable benefits in terms of its sensitivity and ability to monitor in real-time. However, it may need specialised equipment and consideration of surface conditions.

CHAPTER THREE THEORY

Lord Kelvin provided a theoretical description in 1853 (Thomson W.). The relationship is expressed as follows (Harwood N, Cummings WM)

$$\delta T = -\frac{\alpha}{\rho C_p} T \delta\sigma \qquad (1)$$

Where, δT is the temperature changes, T is the absolute temperature, α is the coefficient of thermal expansion, ρ is the mass density, C_p is the Specific heat at constant pressure, $\delta\sigma$ is the change in scalar sum of the principal stresses

Experiment was undergone in elastic region of metal, therefore load applied under its yield strength. Temperature developed in the damage location eventually proportional to sum of two principal stresses. A signal which is represented as a sinusoidal wave can be written as

$$y\,(t) = A \sin(\,\omega t + \emptyset) \qquad (2)$$

Where, A is the amplitude, ω is the angular velocity and ∅ is the phase offset. Temperature readings was recorded at two locations. First one is in plane amplitude and second one is quadrature amplitude

The in-plane amplitude of the temperature referred to the measurement of temperature amplitude was taken when the load signal reached its maximum value. It can be represented:

$$y\,(t) = A \cos(\omega t + \emptyset) \qquad (3)$$

On the other hand, the quadrature amplitude of the temperature referred to the measurement of temperature amplitude was taken when the load signal reached its average value, which is zero. It can be represented:

$$y\,(t) = A \sin(\omega t + \emptyset) \qquad (4)$$

They are the same signal but shifted in phase by 90 degrees. The in-plane amplitude is directly proportional to the peak amplitude of the stress sum at a particular location on the structure. Whereas in quadrature amplitude stress concentration is higher to visualize in a plotting result.

CHAPTER FOUR EXPERIMENTAL STUDY

A detailed discussion of the experimental design used in this study to apply the TSA approach. The experimental setup to examine the impacts of changing parameters on the detectability of the damages was covered as one of the important elements under consideration for assessing the efficacy of employing the TSA approach for damage detection. In order to guarantee the reproducibility of the tests, the parameters of the test specimen and the apparatus were also be established. The primary tests conducted for this study include a cyclic bending loading of a mild steel beam with internal flaws at different parameter values.

Lastly, Ansys Workbench 2023 software was used to perform a Finite Element Analysis of the cyclic bending loading test of a mild steel beam with damages at various parameters and boundary conditions.

Preparation of specimen

For the experiment, mild steel was selected as the material for the specimens. The dimensions of the specimens were 500 mm in length, 25 mm in width, and 6 mm in thickness. A total of five specimens were utilized during the experimental procedure, with depths of 1 mm, 1.5 mm, 2 mm, 2.5 mm, and 3 mm, respectively.

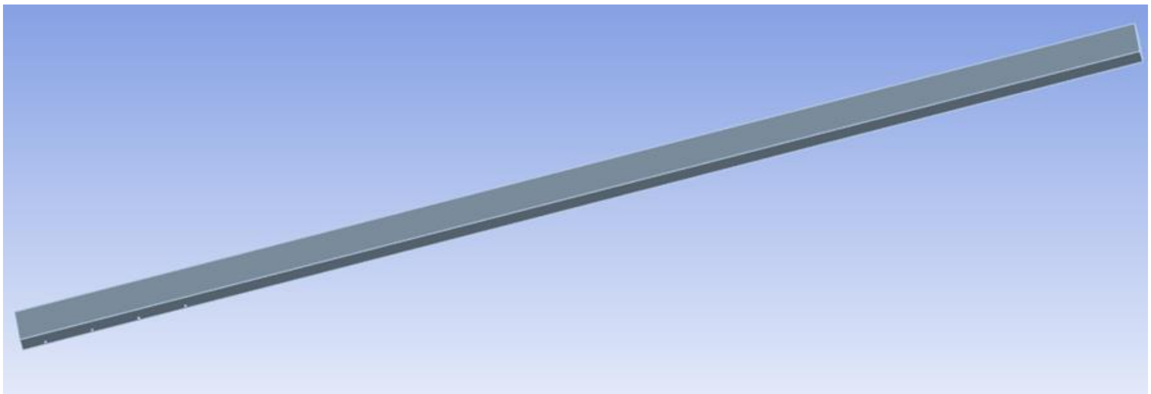

Figure 1 Specimen

There was total four holes in each specimen. First hole distance from bottom was 12.5mm, second, third- and fourth-holes distance from bottom were 37.5, 62.5 and 87.5mm respectively. From bottom 100 mm along with its length was examined under damage detection. Rest of the part of specimen was not assess the investigation of TSA.

Experimental setup

The experimental setup comprised the following equipment: an LDS V830 shaker, a control panel, a blower, a data acquisition system, an infrared camera, a computer, a laptop, and cables. The LDS V830 shaker system is specifically designed for vibration and mechanical shock testing, utilizing sinusoidal, random, or transient excitation. It has a total weight of 616 kg and is capable of generating frequencies up to 3000 Hz. A detailed flow diagram of the setup is provided in the appendix A (figure 19 and 20). The infrared camera was positioned in front of the specimen to capture clear images for the TSA experiment. The laptop and computer were used to input data into the control panel and to collect data via the data acquisition system. The specimens were subjected to a cyclic bending load using an LDS V830, the temperature gradient was recorded using an infrared camera and the data from the infrared camera was collected and recorded using a data acquisition system and MiTE software. The experimental setup for this experiment is shown in Figure 2.

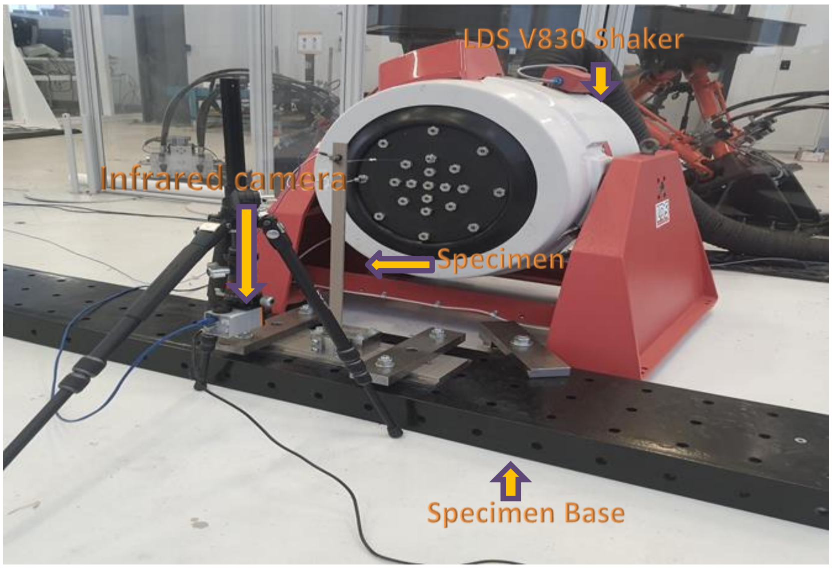

Figure 2 Experimental setup

It was crucial to check that the infrared camera was focused on the specimen's surface (the bottom 100 mm) before beginning the experiment. This was accomplished by employing a magnet to secure a thin metal ruler to the specimen's surface. Specimen was needed to fixed in the ground. Needed to make sure that there was no attachment with shaker and specimen. A blower was connected with shaker so that it can maintain a certain temperature inside for better and safe performance. Control panel was connected with computer and shaker. From computer it was commended the frequencies and voltage. And this commend was operated by shaker through control panel.

Displacement was primary component which was showing in computer as a result of frequencies and voltage. The below formula was applied to get acceleration from displacement and frequencies.

$$a = w^2 s$$

Where, $a =$ Acceleration, ω = Frequency and s = Displacement

During the experiment, frequencies ranging from 2 Hz to 20 Hz were applied to various specimens to observe their displacement. This displacement was recorded for subsequent analysis. To achieve this, a voltage between approximately 0.01 V and 0.2 V was applied to the shaker via the control panel. The table 1 was summery of experimental inputs carry out.

Test parameters	Values
Frequency	2 Hz, 4 Hz, 6 Hz, 8 Hz, 10 Hz, 15 Hz, 20 Hz
Depth /Specimen	1 mm, 1.5 mm, 2mm, 2.5 mm, 3 mm
Voltage	0.01 v to 0.2v
Displacement	4 mm, 8mm, 12 mm, 16 mm and 20 mm

Table 1 Experimental time data

Data collection was conducted using an accelerometer, data acquisition system, and either a computer or laptop. This process was divided into two stages: the first involved data from the LDS shaker, and the second involved data from the infrared camera. Data from the shaker were transmitted through the accelerometer to the data acquisition system, and subsequently to the computer. Data from the infrared camera were collected directly via the laptop. Mite and MATLAB software were employed to process the final data and generate graphs. The figure below illustrates the data collection process from both the infrared camera and the shaker.

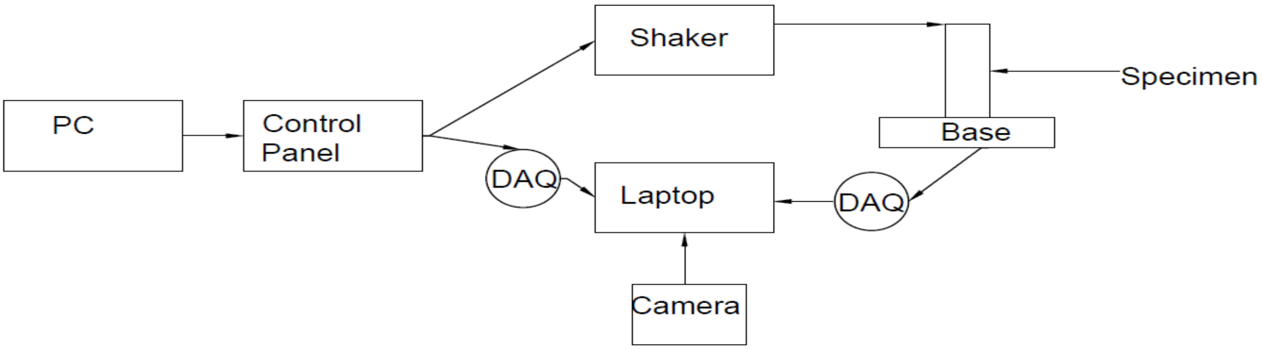

Figure 3 Data flow diagram

Finite element analysis

Computerized methods like as finite element analysis (FEA) may be utilized for predicting a product's response to physical influences such as heat, vibration, force, fluid flow, and others that occurs in the real world.ANSYS workbench 2023R was used in this project to make model. So far for this project, 5 models were done for each specimen. That's mean total 25 models were made so far.

The equation below was used in the Finite Element Analysis (FEA) model to transform the findings of the Structural FEA model into the Thermal response.

$$k\nabla^2 T - \rho\,.\,C_p \frac{\partial T}{\partial t} = T_o\,\alpha \frac{\partial \sigma_1}{\partial t} \tag{5}$$

Where, k is the thermal conductivity, ρ is the material Density, T_o is the absolute Temperature, T is the Temperature field, σ_1 is the first stress invariant and α is the coefficient of thermal expansion

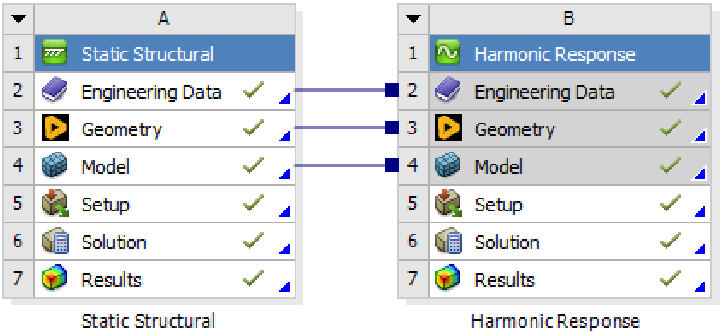

Figure 4 ANSYS workbench 2023

CHAPTER FIVE NUMERICAL STUDY

TSA Experiment

As stated in the methodology section, MiTE software was used to record temperature data during the cyclic bending loading tests. The load signal was also provided to the computer as a reference signal in order to determine the phase lag between the load signal and the thermal response curve. Thermoelastic Response Signal, or TRS, as it will be called in this thesis, is a proportional correlation to temperature variations caused by the thermoelastic effect. The thermal response data obtained from the infrared camera using MiTE software. The temperature fluctuation caused by the thermoelastic effect at a certain place is directly related to the amplitude (A) of TRS, and this in turn is directly related to the stresses in the beam.

Cyclic bending loading experiment

Using data from an infrared camera, MiTE software collected images of the in-plane amplitude (X) and quadrature amplitude (Y) of a beam with holes at a depth of 1 mm during cyclic bending loading tests. The beam's had constant displacement 10 mm and the frequency was 15 Hz.

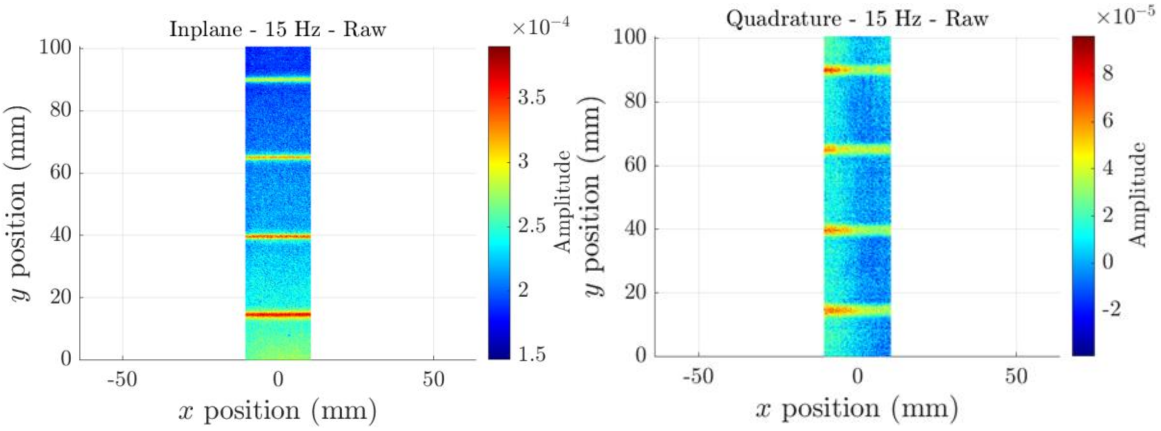

Figure 5 In phase and Quadrature images generated by infrared camera

The thermoelastic response signal appears to be more amplified at the sites of the holes, as demonstrated by the noticeable darker lines in the photos, making both the quadrature and in-phase views highly promising. MATLAB script was created to handle these pictures. First, as shown in Figure 5, the TRS in-phase amplitude (X) values at the beam's bottom were plotted against the point along the beam's length. Images produced by an infrared camera in both in phase and quadrature.

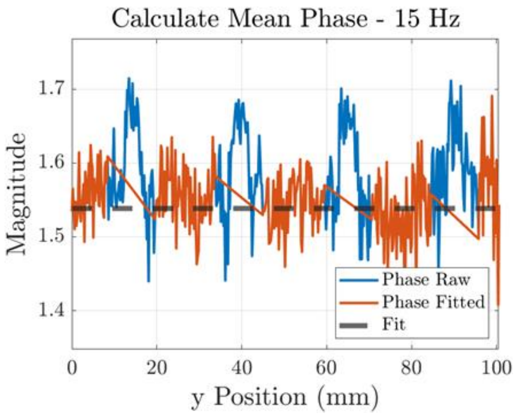

Figure 6 In plane amplitude of TRS along a single line at the centre of the beam

The plots in Figure 6, shows at 15 Hz calculated mean phase between magnitude 1.5 and 1.6 and position of holes phase raw which approximate 1.7 magnitude peak. Upon visual inspection of the plot, the peaks can be easily distinguished, despite some noise being present. This can represent the holes and position of holes where 1.7 magnitude was observed.

Effect of varying frequencies

1 mm depth specimen and with 10 mm constant displacement was examined at 5 Hz, 6 Hz, 8 Hz, 10 Hz, and 15 Hz frequencies to observe the impact of changing load signal frequencies on the TRS measured by the infrared camera. Plotting the TRS magnitude with in-phase amplitude and quadrature amplitude values against the beam length position (100 mm from bottom) for each frequency in a single graph is shown in Figure 7.

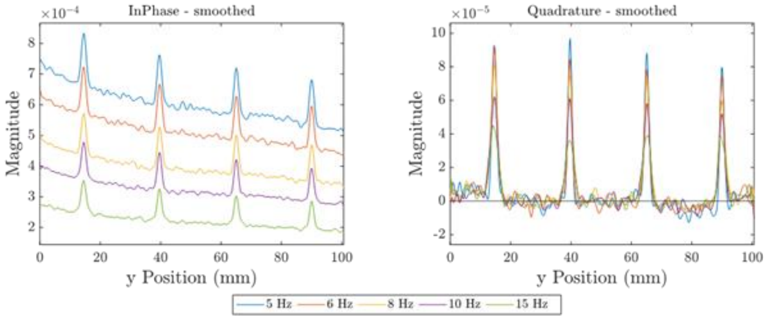

Figure 7 TRS magnitude values of the beam with varying frequencies

Each frequency has base amplitude levels that are as follows: 15 Hz < 10 Hz < 8 Hz < 6 Hz < 5 Hz. Interestingly, though, each frequency's peak heights in relation to its base level are arranged in descending sequence. Both in phase and quadrature are showing peak at the position of holes, however quadrature amplitude is showing high peak which is very easy to identify damages.

Effect of varying displacement

1 mm depth specimen with constant frequency 10 Hz was examined at 2 mm, 4 mm, 6mm, 8mm, 10mm, 12 mm, 14mm, 16mm, 18mm and 20 mm displacement amplitudes as stated in order to see the impact of changing displacement signal amplitudes on the TRS magnitude captured by the infrared camera. The TRS in-plane amplitude values are plotted against the beam's length (100 mm from bottom) for each displacement amplitude in the same graph, as shown in Figure 9.

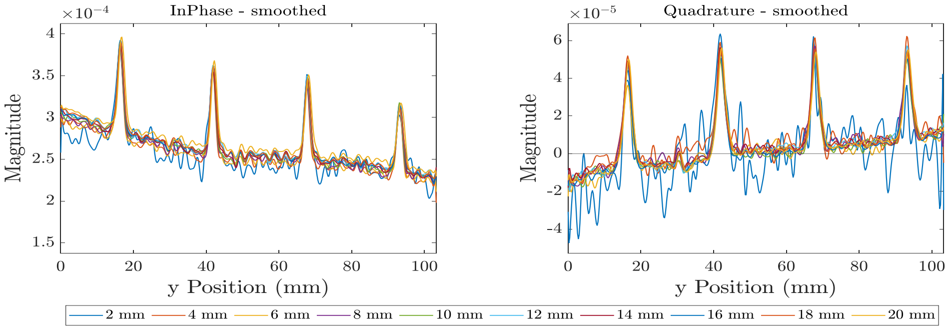

Figure 8 TRS magnitude values at the bottom of the beam for varying displacement amplitudes

The graph from figure 8 demonstrates that y position of beams where holes are sustained, TRS values is increasing in that position. In phase smooth data graph, first hole position's TRS value approximate 4×10^{-4} and forth (last) hole position's TRS value approximate 3.2×10^{-4}. However, quadrature sooth data graph, first hole position's TRS value approximate 5×10^{-5} and forth (last) hole position's TRS value approximate 6×10^{-5}. In quadrature amplitude TRS magnitude in the position of holes are giving better peaks. In this both in phase and quadrature amplitude 2 mm displacement signal gave much noise than others signal. When displacement was being increased, noise level was being reduced as observed from both graphs.

FEA results

Ansys Workbench 2023 software used to create models for testing how materials respond to repeated loading from one direction at different frequencies. Then compared these computer-generated results to real-world test data to see if models were accurate. The figure 9 illustrates how temperature changes were represented in simulated models.

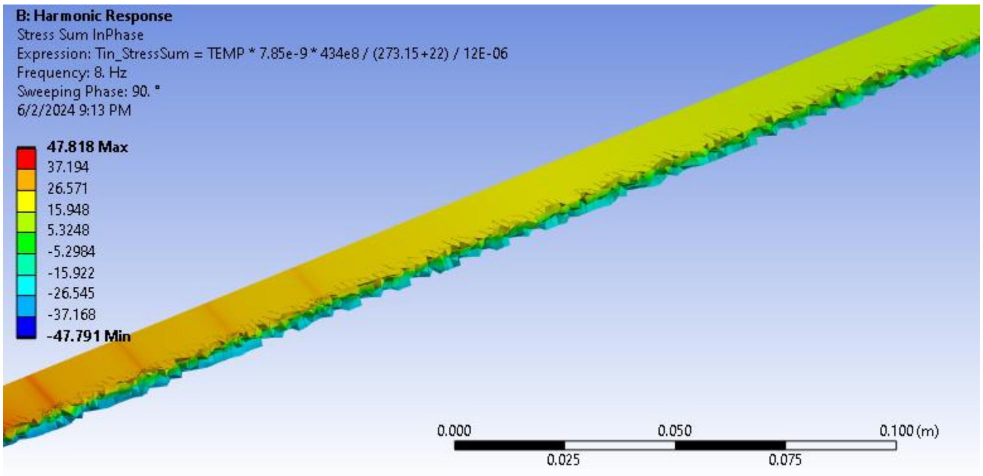

Figure 9 Temperature variation visualized in the FEA model at 8Hz

The figure 10 displays how temperature changes across the length of the beam in Finite Element Analysis (FEA) model, comparing different frequencies of cyclic bending loading. By selecting patch confirming method as mesh sizing, geometry of model looked unfinished and rough surface.It closely mirrors the patterns seen in the actual test results shown in another figure 7, supporting the accuracy of FEA model. Peaks in beams in FEA simulation is proved that damage location is identified by FEA exactly in the same position where it has hole. In appendices C, all the figures are showed which were done in ANSYS workbench.

However, there are discrepancies between this graph and the actual test results for varying frequencies. The peaks in temperature relative to the baseline increase proportionally with higher frequencies in the model, which differs from the observed behaviour in the real-world results.

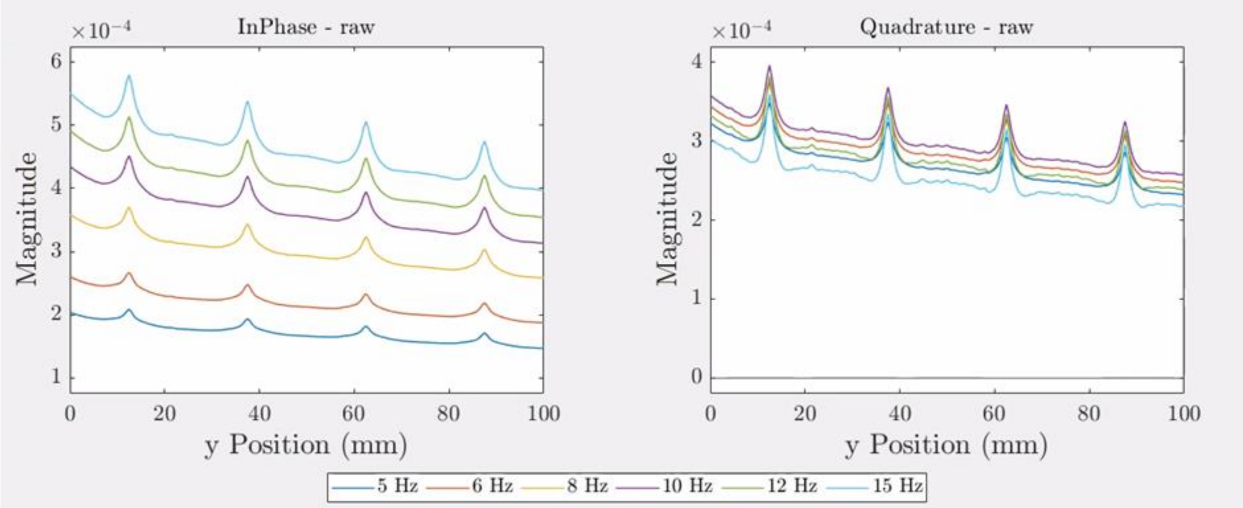

Figure 10 In-plane temperature variation results of the FEA model for varying frequencies.

CHAPTER SIX COMPERATIVE ANALYSIS

When a material is subjected to cyclic loading, as the thermoelastic effect explains, temperature fluctuations occur. In adiabatic circumstances, the temperature change in isotropic materials precisely corresponds with the total of the two major stresses acting on the surface. As a result, the TSA approach may be utilised to detect the stress field on the surface of a loaded element utilising this temperature fluctuation which is proportional to each other. This stress field may be examined to find areas of intense stress, which might point to flaws or damage in the loaded part. Since the peak amplitude of the stress sum at a particular location on the structure is closely connected to the in-plane amplitude, most of the findings are shown for the TRS in-plane amplitudes obtained from the tests.

Different frequencies

Figure11, represents frequencies behaviour in the terms of TRS amplitude. In figure 11, baseline noise within the data when excluding the peaks as frequencies are increasing and at the same time the magnitude of both in phase and quadrature values of TRS is decreased. In phase TRS magnitude values surprisingly fall after 2 Hz frequencies, however quadrature magnitude of TRS is showing much stable. At lower frequencies sharpness of peak from figure is looking more dominated than sharpness of peak in higher frequencies. However, at higher frequencies existing of noise is less.

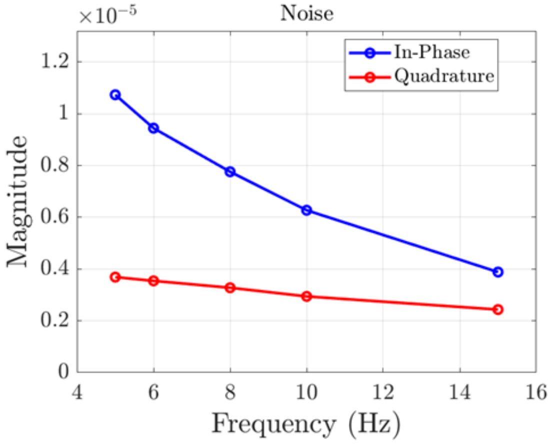

Figure 11 Base line noise within the data when excluding peaks

Noise level is more dominated in lower-level frequencies that is observed in figure 12. It is observed that both in phase and quadrature amplitude, when frequencies are getting higher noise level is reducing.

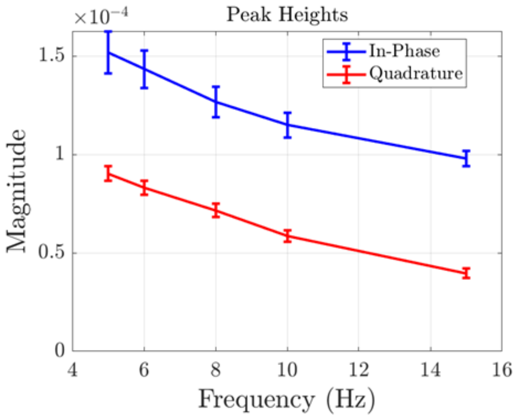

Figure 12 Peak height - error bars represent the noise within the smoothed data

The distribution of TRS amplitudes vs frequency in Figure 7 and 10 shows that, in contrast to the load amplitude, the TRS output does not correlate to the frequency of the load signal in a proportionate or linear way. The natural frequency of the part being examined may determine the ideal frequency level for reaching the highest TRS amplitude values utilising the TSA technique. Further investigation is necessary to get definitive conclusions on the ideal frequency level to attain the highest and desirable results.

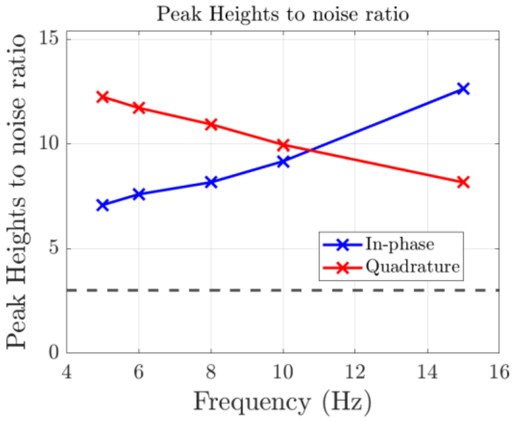

Figure 13 Peak height to noise ratio

In phase amplitude and quadrature amplitude are both going opposite direction in the terms of peak height and noise ration. Consequently, it is clear that a lower frequency is preferred for employing the TSA approach to identify internal faults even though the mean TRS amplitude does not correlate to the frequency level in a linear fashion. However, it has also been noticed that noise involvement higher in lower frequencies.

Different Deflection

Observing displacement curve in figure 8, TRS magnitude is more dominated when beam structure is deflected high displacement. In the terms of displacement analysis, 1 mm depth specimen with constant frequency 10 Hz, lower displacement of specimen is showing very high noise level than higher displacement. In below figure 14, when noise within the data is excluding the peaks are surprising getting low after 2mm displacement and after 4 mm displacement of beam in a certain frequencies TRS values are almost 0.5×10^{-5} at in phase amplitude and 0.2×10^{-5} at quadrature amplitude.

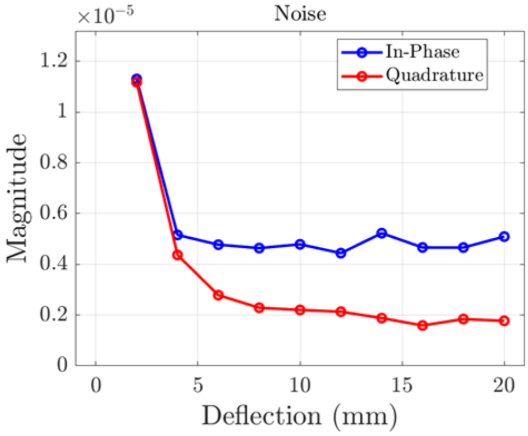

Figure 14 Noise within data when excluding peaks

In figure 15, it is showing peak heights where error bars represent the noise within the smoothed data. However, it is cleared that when deflection is low, noise in the system is high and when deflection is high noise in the system is getting low. In both in phase and quadrature amplitude this property is same. However, quadrature values of TRS are lower than in phase TRS value. At 2 mm deflection, noise bar is too much high that indicate that at lower displacement below or equal 2 mm, noise level will be high. Quadrature amplitude is showing much more better results than in phase amplitude regarding noise presence in signals.

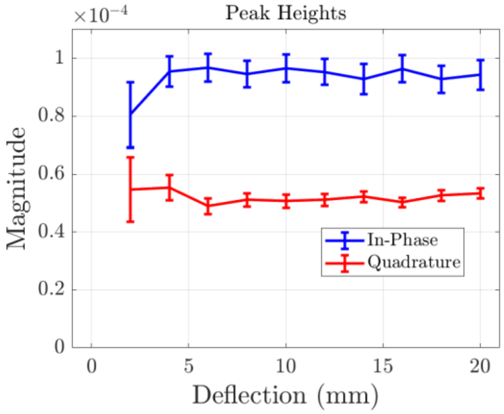

Figure 15 Peaks heights - error bars represent the noise within the smoothed data

In figure 16, peak height to noise ratio is getting higher with increasing deflection. Both in phase and quadrature are getting higher ratio as deflection is being increased.

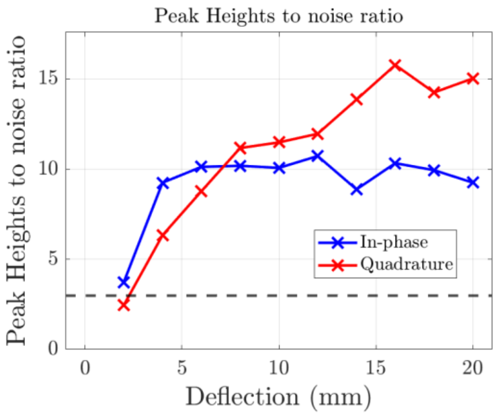

Figure 16 Peak height to noise ratio

Discussion for FEA

In summary, the FEA model effectively reflects the actual experimental data from the cyclic bending loading test, accurately pinpointing the damage location on the beam, which was main objective. However, with increasing and decreasing frequencies, models are not showing exact scenario. This highlights the necessity for additional research to validate the impact of frequency and underscores the need for further refinement of the model.

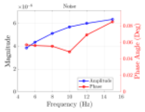

Figure 17 Peak heights in FEA results with different frequencies

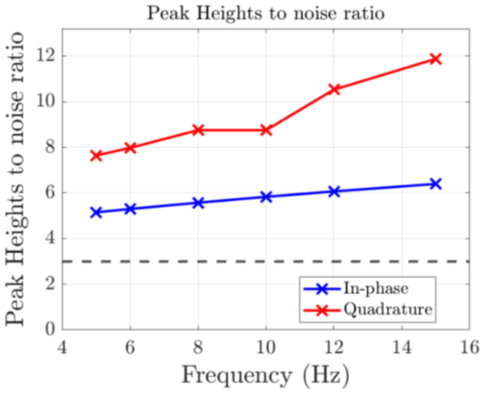

Figure 18 Peak height to noise ratio from FEA

In figure 17, it is noticeable that for both amplitude and phase, magnitude is increasing with increasing frequencies. At frequency 10 Hz at phase suddenly drops. However, at amplitude noise bar is increased by increasing frequencies. In figure 18, peak heights to noise ratio are increased with increasing frequencies. Surprisingly quadrature values look dominating rather than in phase in FEA results whereas in real experiment in phase values was dominating.

CHAPTER SEVEN CONCLUSION AND FUTURE WORK

Conclusion

According to the analysis of data from the uniaxial cyclic loading experiment, the TSA method proves to be a highly effective technique for accurately identifying internal faults within metal structural elements at specific loading amplitudes and frequency levels. The findings suggest that lower load amplitudes improve the detectability of damage, potentially facilitating the identification of internal flaws located deeper beneath the surface being inspected. Furthermore, it was observed that quadrature amplitude measurements are more effective for detecting surface damages at greater depths from the spotted outer surface, whereas in-plane amplitude measurements are more suited for identifying internal damages.

Further research is necessary to comprehensively understand the non-linear relationship between load signal frequency and TRS amplitude levels. Although evidence indicates that higher load signal frequencies improve TSA's ability to detect internal defects amidst noise, the precise nature of this relationship remains unclear. Additionally, while the FEA model accurately represents variable uniaxial loading conditions, it fails to adequately capture the effects of varying load signal frequencies, highlighting the need for further investigation in this area. Overall, this study provides substantial evidence that the TSA method is a highly effective whole-field non-destructive testing (NDT) technique for identifying internal flaws in metals.

Future Work

Further research is essential to gain a more comprehensive understanding of how altering load signal frequency influences the TSA method's effectiveness in damage detection, as discussed in the comparative study and Conclusion sections. To substantiate the statistical findings and obtain definitive evidence, it is necessary to investigate the TSA method's performance in uniaxial loading scenarios with higher load amplitudes. Additional variables, such as the defect's size or volume, the material of the structural member, and environmental conditions, may also impact the TSA method's capability to detect internal defects. Examining these factors will contribute to a more thorough evaluation of the TSA technique's strengths and limitations in defect detection.

REFERENCE

1. Ryall, T.G. and Wong, A.K., 1993. Infrared staring arrays and digital signal processing. In *PROCEEDINGS OF THE SEM SPRING CONFERENCE ON EXPERIMENTAL MECHANICS* (pp. 730-730). SEM SOCIETY FOR EXPERIMENTAL MECHANICS INC.
2. Lesniak, J.R. and Boyce, B.R., 1994, June. A high-speed differential thermographic camera. In *SEM Spring Conference Proceedings, Baltimore, Maryland* (pp. 491-497).
3. Civera, Marco, and Cecilia Surace. "Non-Destructive Techniques for the Condition and Structural Health Monitoring of Wind Turbines: A Literature Review of the Last 20 Years." *Sensors*, vol. 22, no. 4, 18 Feb. 2022, p. 1627, https://doi.org/10.3390/s22041627.
4. Di Carolo, Francesca, et al. "A Thermoelastic Stress Analysis General Model: Study of the Influence of Biaxial Residual Stress on Aluminium and Titanium." *Metals*, vol. 9, no. 6, 10 June 2019, p. 671, https://doi.org/10.3390/met9060671. Accessed 11 Dec. 2019.
5. Dwivedi, Sandeep Kumar, et al. "Advances and Researches on Non Destructive Testing: A Review." *Materials Today: Proceedings*, vol. 5, no. 2, 2018, pp. 3690–3698, www.sciencedirect.com/science/article/pii/S2214785317328936, https://doi.org/10.1016/j.matpr.2017.11.620. Accessed 28 Nov. 2019.
6. Gdoutos, Emmanuel E. *Experimental Mechanics*. Vol. 269, Springer Nature, 15 Nov. 2021.

---. "Thermoelastic Stress Analysis (TSA)." *Solid Mechanics and Its Applications*, 16 Nov. 2021, pp. 261–267, https://doi.org/10.1007/978-3-030-89466-5_13. Accessed 1 June 2024.

7. Ma, Yufei, et al. "Ultra-High Sensitive Trace Gas Detection Based on Light-Induced Thermoelastic Spectroscopy and a Custom Quartz Tuning Fork." *Applied Physics Letters*, vol. 116, no. 1, 6 Jan. 2020, polysense.poliba.it/wp-content/uploads/2020/01/111_QEPTS_APL_2020.pdf, https://doi.org/10.1063/1.5129014. Accessed 1 June 2024.
8. Harwood, N. and Cummings, W.M. (1991). *Thermoelastic Stress Analysis*. CRC Press.
9. Rajic, N. and Rowlands, D. (2013). Thermoelastic stress analysis with a compact low-cost

microbolometer system. *Quantitative InfraRed Thermography Journal*, 10(2), pp.135–158. doi:https://doi.org/10.1080/17686733.2013.800688.

10. William Thomson Kelvin (1851). *On the Dynamical Theory of Heat*.

11. Muzika, L., Švantner, M., Houdková, Š. and Šulcová, P., 2021. Application of flash-pulse thermography methods for quantitative thickness inspection of coatings made by different thermal spraying technologies. *Surface and Coatings Technology*, *406*, p.126748.

12. Breitenstein, O. and Langenkamp, M., 2003. Lock-in thermography. *Basics and Use for Functional Diagnostics of Electronics Components*.

13. Gülcan, O., 2022. Recent developments in vibrothermography. *Res Eng Struct Mater*, *8*(1), pp.57-73.

14. Chawla, V., Jayaganthan, R. and Chandra, R., 2008. Finite element analysis of thermal stress in magnetron sputtered Ti coating. *Journal of Materials Processing Technology*, *200*(1-3), pp.205-211.

15. Egilmez, F. and Nalbant, L., 2012. Comparison of the effect of thermal stresses on tooth-colored posts, cores and tooth structures by finite element analysis. *Cumhuriyet Dental Journal*, *15*(2), pp.118-129.

16. Sangwongwanich, A., Wang, H. and Blaabjerg, F., 2020. Reduced-order thermal modeling for photovoltaic inverters considering mission profile dynamics. *IEEE Open Journal of Power Electronics*, *1*, pp.407-419.

17. Chen, X.J., Nakano, S., Liu, L.J. and Kakimoto, K., 2008. Study on thermal stress in a silicon ingot during a unidirectional solidification process. *Journal of Crystal Growth*, *310*(19), pp.4330-4335.

18. Xu, M., Li, T., Yang, M. and Andersson, M., 2016. Solid oxide fuel cell interconnect design optimization considering the thermal stresses. *Science bulletin*, *61*(17), pp.1333-1344.

19. Lin, Q., Zhao, P.F., Yang, R.L. and Wu, H.F., 2024. Thermal Characteristic Investigation for a Multichip Module Based on APDL. *International Journal of RF and Microwave Computer‐Aided Engineering*, *2024*(1), p.2028369.

20. Makoto, H. and Akihiko, H., 2012. High Cycle Thermal Fatigue Crack Initiation and Growth Behavior

in a Simulated BWR Environment. *JSMME*, *6*(10), pp.989-1001.

21. Zhang, Y., Hou, C., Jin, X., Li, D., Zhao, L., Yang, L. and Fan, X., 2024. Thermal fatigue crack initiation and propagation behaviors of GH3230 nickel-based superalloy. *Fatigue & Fracture of Engineering Materials & Structures*, *47*(1), pp.6-19.

22. Xia, P., Yang, L., Yu, J., Sun, X., Guan, H. and Hu, Z., 2011. Influence of direction of notch on thermal fatigue property of a directionally solidified nickel base superalloy. *Rare Metals*, *30*, pp.472-476.

APPENDICES

Appendices A

Figure 19 V830 Shaker

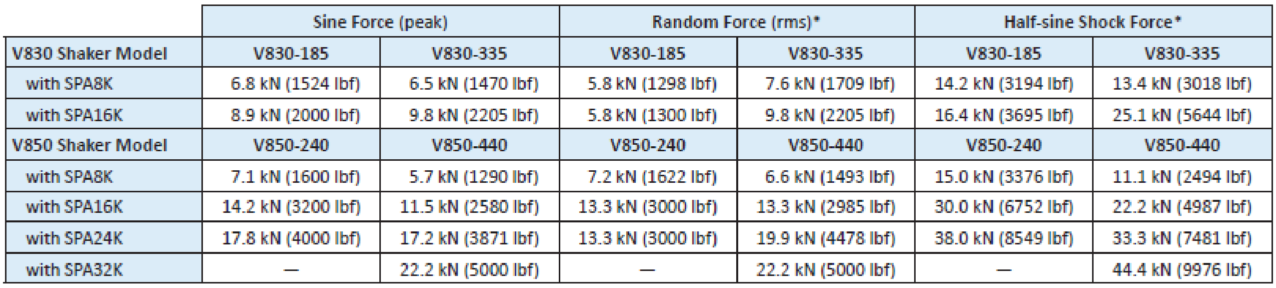

	Sine Force (peak)		Random Force (rms)*		Half-sine Shock Force*	
V830 Shaker Model	V830-185	V830-335	V830-185	V830-335	V830-185	V830-335
with SPA8K	6.8 kN (1524 lbf)	6.5 kN (1470 lbf)	5.8 kN (1298 lbf)	7.6 kN (1709 lbf)	14.2 kN (3194 lbf)	13.4 kN (3018 lbf)
with SPA16K	8.9 kN (2000 lbf)	9.8 kN (2205 lbf)	5.8 kN (1300 lbf)	9.8 kN (2205 lbf)	16.4 kN (3695 lbf)	25.1 kN (5644 lbf)
V850 Shaker Model	V850-240	V850-440	V850-240	V850-440	V850-240	V850-440
with SPA8K	7.1 kN (1600 lbf)	5.7 kN (1290 lbf)	7.2 kN (1622 lbf)	6.6 kN (1493 lbf)	15.0 kN (3376 lbf)	11.1 kN (2494 lbf)
with SPA16K	14.2 kN (3200 lbf)	11.5 kN (2580 lbf)	13.3 kN (3000 lbf)	13.3 kN (2985 lbf)	30.0 kN (6752 lbf)	22.2 kN (4987 lbf)
with SPA24K	17.8 kN (4000 lbf)	17.2 kN (3871 lbf)	13.3 kN (3000 lbf)	19.9 kN (4478 lbf)	38.0 kN (8549 lbf)	33.3 kN (7481 lbf)
with SPA32K	—	22.2 kN (5000 lbf)	—	22.2 kN (5000 lbf)	—	44.4 kN (9976 lbf)

Table 2 V830 shaker maximum force ratings

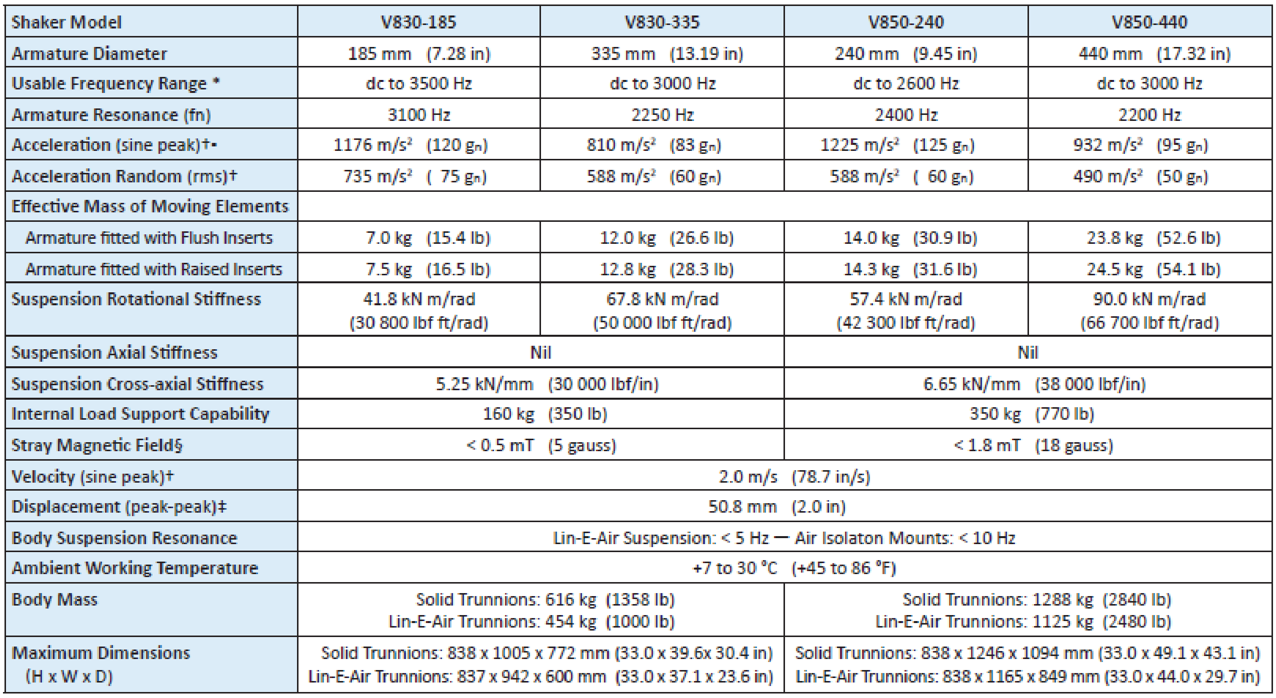

Shaker Model	V830-185	V830-335	V850-240	V850-440
Armature Diameter	185 mm (7.28 in)	335 mm (13.19 in)	240 mm (9.45 in)	440 mm (17.32 in)
Usable Frequency Range *	dc to 3500 Hz	dc to 3000 Hz	dc to 2600 Hz	dc to 3000 Hz
Armature Resonance (fn)	3100 Hz	2250 Hz	2400 Hz	2200 Hz
Acceleration (sine peak)†•	1176 m/s^2 (120 g_n)	810 m/s^2 (83 g_n)	1225 m/s^2 (125 g_n)	932 m/s^2 (95 g_n)
Acceleration Random (rms)†	735 m/s^2 (75 g_n)	588 m/s^2 (60 g_n)	588 m/s^2 (60 g_n)	490 m/s^2 (50 g_n)
Effective Mass of Moving Elements				
Armature fitted with Flush Inserts	7.0 kg (15.4 lb)	12.0 kg (26.6 lb)	14.0 kg (30.9 lb)	23.8 kg (52.6 lb)
Armature fitted with Raised Inserts	7.5 kg (16.5 lb)	12.8 kg (28.3 lb)	14.3 kg (31.6 lb)	24.5 kg (54.1 lb)
Suspension Rotational Stiffness	41.8 kN m/rad (30 800 lbf ft/rad)	67.8 kN m/rad (50 000 lbf ft/rad)	57.4 kN m/rad (42 300 lbf ft/rad)	90.0 kN m/rad (66 700 lbf ft/rad)
Suspension Axial Stiffness	Nil		Nil	
Suspension Cross-axial Stiffness	5.25 kN/mm (30 000 lbf/in)		6.65 kN/mm (38 000 lbf/in)	
Internal Load Support Capability	160 kg (350 lb)		350 kg (770 lb)	
Stray Magnetic Field§	< 0.5 mT (5 gauss)		< 1.8 mT (18 gauss)	
Velocity (sine peak)†	2.0 m/s (78.7 in/s)			
Displacement (peak-peak)‡	50.8 mm (2.0 in)			
Body Suspension Resonance	Lin-E-Air Suspension: < 5 Hz — Air Isolaton Mounts: < 10 Hz			
Ambient Working Temperature	+7 to 30 °C (+45 to 86 °F)			
Body Mass	Solid Trunnions: 616 kg (1358 lb) Lin-E-Air Trunnions: 454 kg (1000 lb)		Solid Trunnions: 1288 kg (2840 lb) Lin-E-Air Trunnions: 1125 kg (2480 lb)	
Maximum Dimensions (H x W x D)	Solid Trunnions: 838 x 1005 x 772 mm (33.0 x 39.6x 30.4 in) Lin-E-Air Trunnions: 837 x 942 x 600 mm (33.0 x 37.1 x 23.6 in)		Solid Trunnions: 838 x 1246 x 1094 mm (33.0 x 49.1 x 43.1 in) Lin-E-Air Trunnions: 838 x 1165 x 849 mm (33.0 x 44.0 x 29.7 in)	

Table 3 V830 Shaker specifications

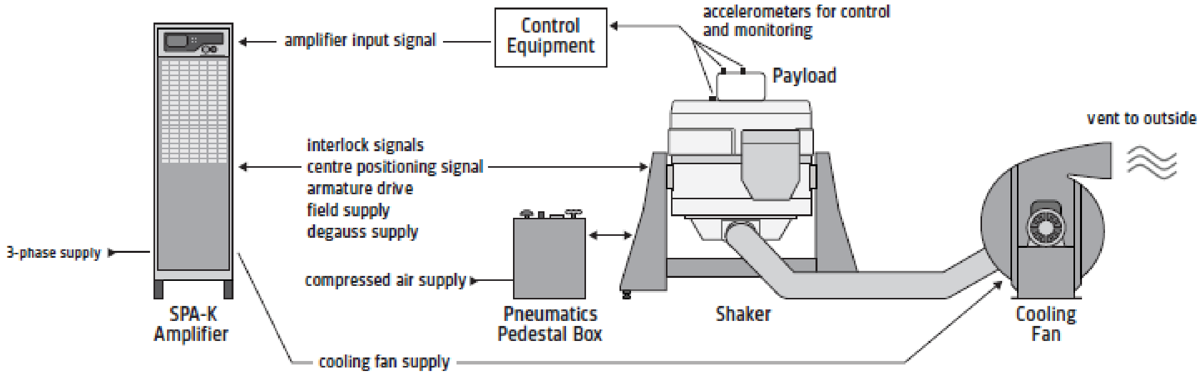

Figure 20 Typical Vibration Test System

Power Range	8 – 32 kVA in 8 kVA increments
Signal-to-Noise Ratio	> 68 dB wrt 100 V rms output**
Input Impedance	10 kΩ nominal
Total Harmonic Distortion	Typically 0.5 to 0.8 % at rated output into rated resistive load
Input Sensitivity	1.0 V for 100 V rms output
Switching Frequency	150 kHz
Efficiency	> 90 % (not including field power supply)
Rated Output Voltage	100 V rms (sine)
Continuous Output Current	80 A rms (sine and random) per 8 kVA increment
Full Power Bandwidth	20 Hz to 3 kHz
Transient Output Current	240 A per 8 kVA increment for 100 ms
Module Efficiency	93 %
Modulation Range	dc to 10 kHz
Protection	Integral protection to prevent output devices from working outside their specification limit.
Ambient Working Temperature	+5 to 30 °C (+41 to 86 °F)
Max. Dimensions (H x W x D)	1870 x 537 x 825 mm (74 x 21 x 33 in)

Table 4 SPA-K Amplifier Specification

	V830 Cooling Fan 50 Hz	V830 Cooling Fan 60 Hz	V850 Cooling Fan 50 Hz	V850 Cooling Fan 60 Hz
Cooling Fan without Silencer (H x W x D)	750 x 683 x 551 mm (29.5 x 28.9 x 21.7 in)	750 x 645 x 551 mm (29.5 x 25.4 x 21.7 in)	914 x 783 x 644 mm (36.0 x 30.8 x 25.4 in)	782 x 705 x 627 mm (30.8 x 27.8 x 24.7 in)
Cooling Fan with Silencer (H x W x D)	824 x 1083 x 551 mm (32.4 x 42.6 x 21.7 in)	824 x 1045 x 551 mm (32.4 x 41.4 x 21.7 in)	991 x 1283 x 648 mm (39.0 x 50.5 x 25.5 in)	873 x 1205 x 639 mm (34.4 x 47.4 x 25.2 in)
Shipping Weight	84 kg (185 lb)	84 kg (165 lb)	130 kg (287 lb)	130 kg (287 lb)

Table 5 Cooling fan/ blower specification

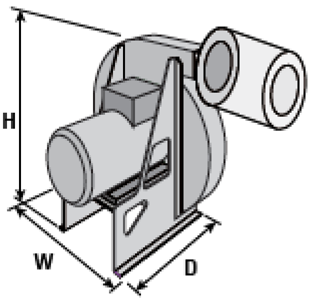

Figure 21 Cooling fan/ blower

Appendices B

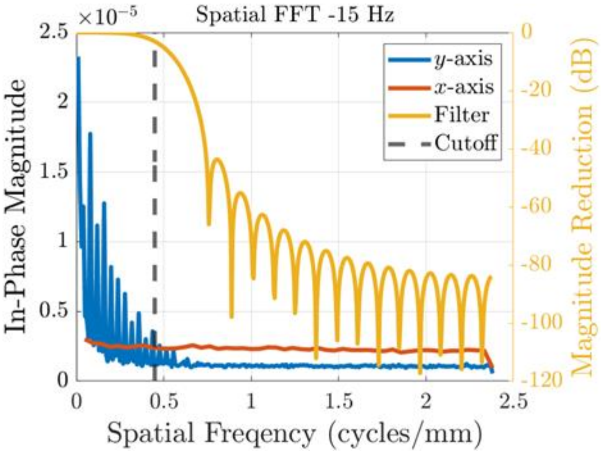

Figure 22 The spatial filter uses to remove the noise from the thermal image

Spatial filters are frequently employed to eliminate noise from images. One common method involves replacing the value of a pixel with the average value of its neighbouring pixels. While this approach is effective at reducing random noise, it can also result in blurring sharp edges within the image. Alternatively, a filter can replace the value of a pixel with the median value of its neighbours. This median filter is often more effective than the mean filter in preserving edges, although it may not be as efficient at reducing noise.

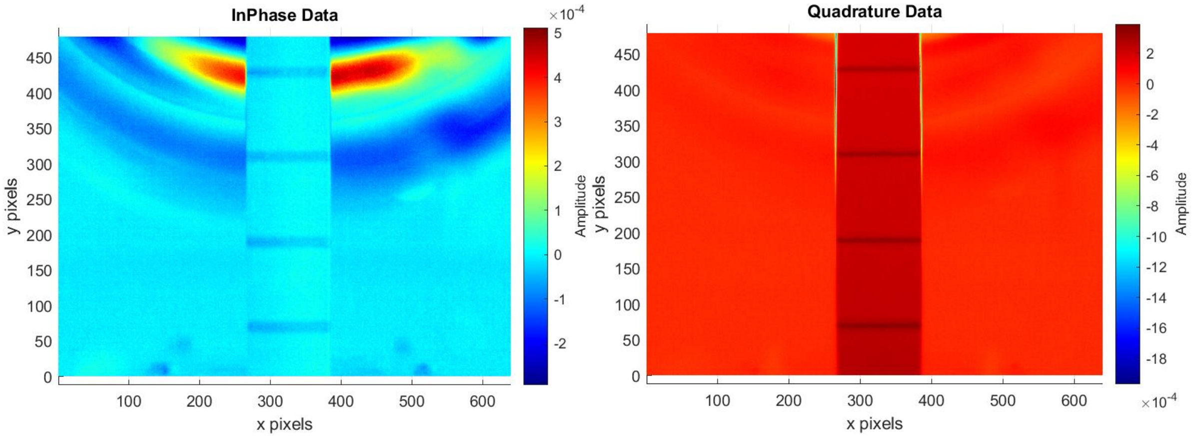

Figure 23 Original Data from the camera

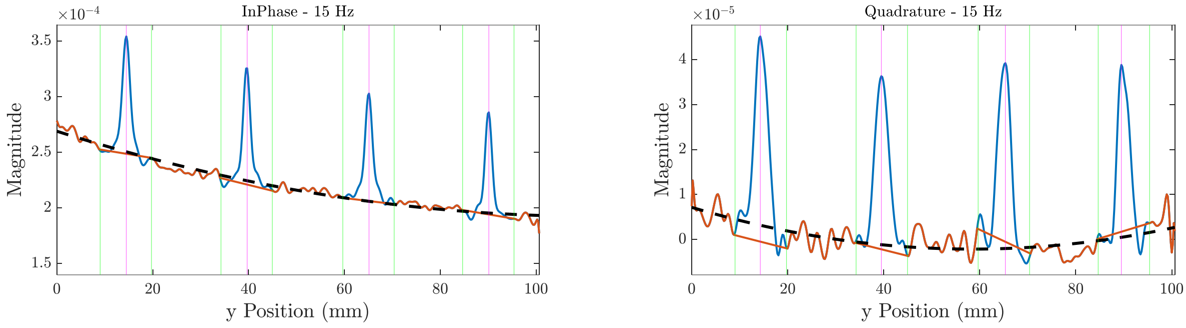

Figure 24 Baseline Noise within the data when excluding the peaks.

Appendices C

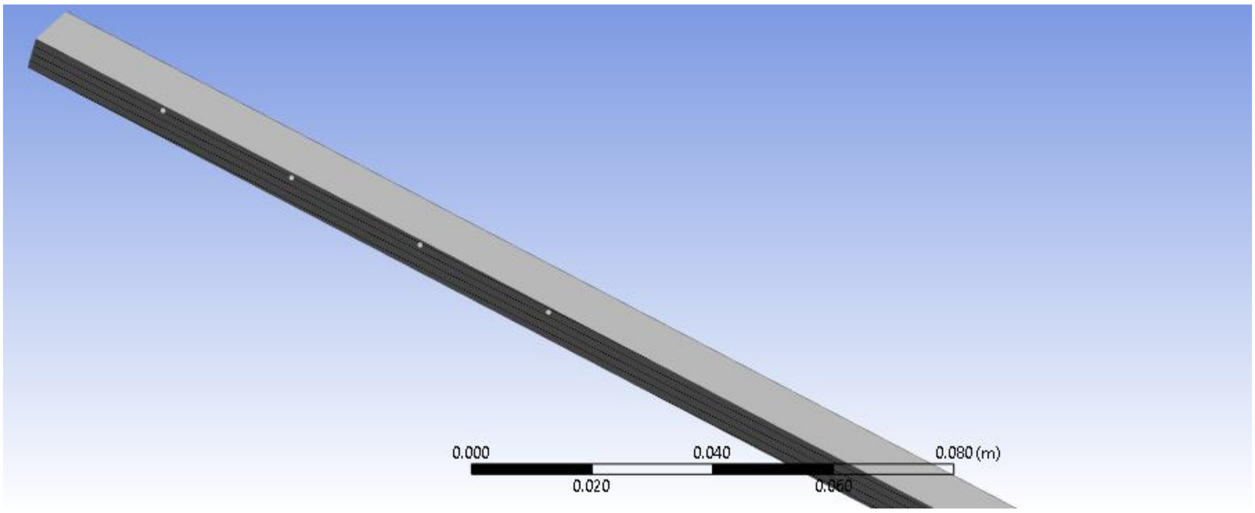

Figure 25 Specimen design in ANSYS workbench

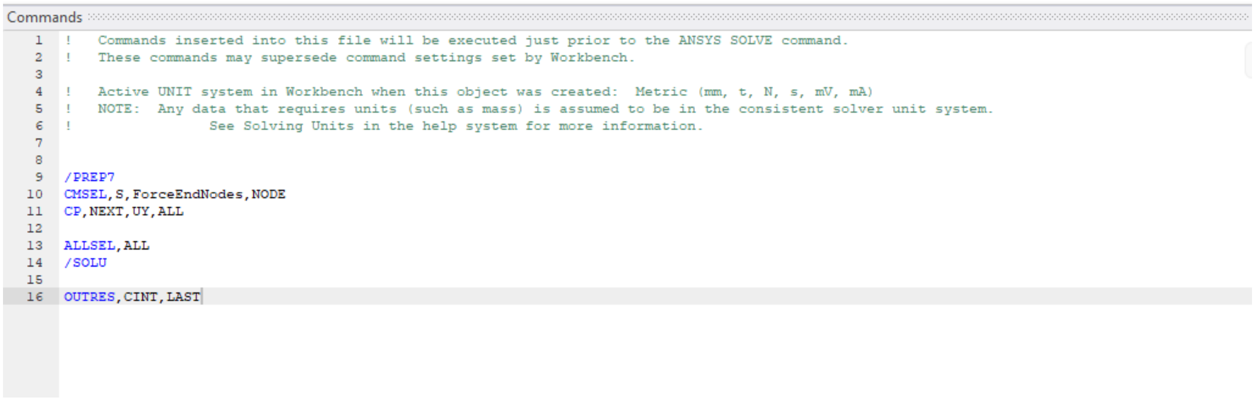

```
!   Commands inserted into this file will be executed just prior to the ANSYS SOLVE command.
!   These commands may supersede command settings set by Workbench.

!   Active UNIT system in Workbench when this object was created:  Metric (mm, t, N, s, mV, mA)
!   NOTE:  Any data that requires units (such as mass) is assumed to be in the consistent solver unit system.
!                See Solving Units in the help system for more information.


/PREP7
CMSEL,S,ForceEndNodes,NODE
CP,NEXT,UY,ALL

ALLSEL,ALL
/SOLU

OUTRES,CINT,LAST
```

Figure 26 Code in ANSYS

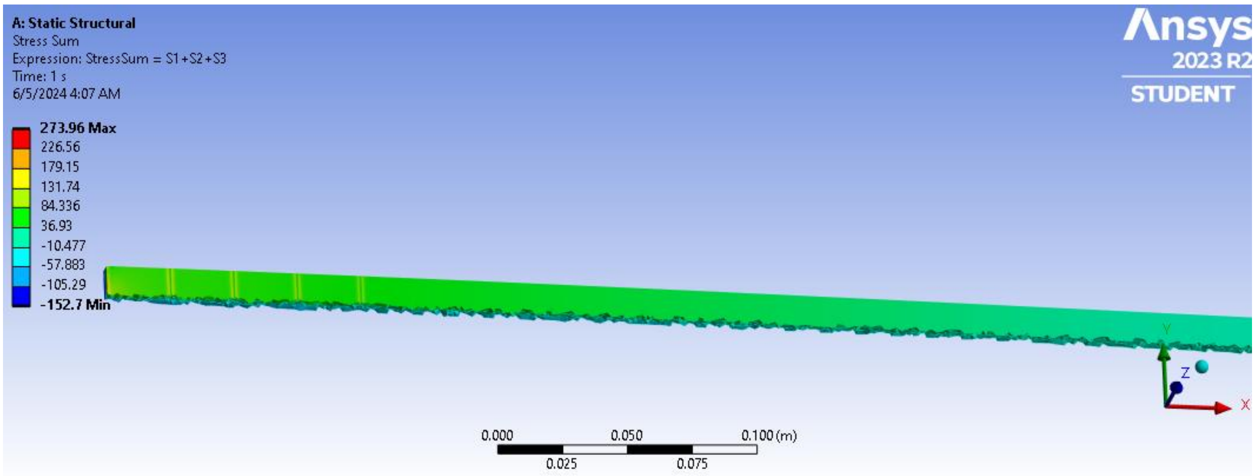

Figure 27 Stress sum in ANSYS

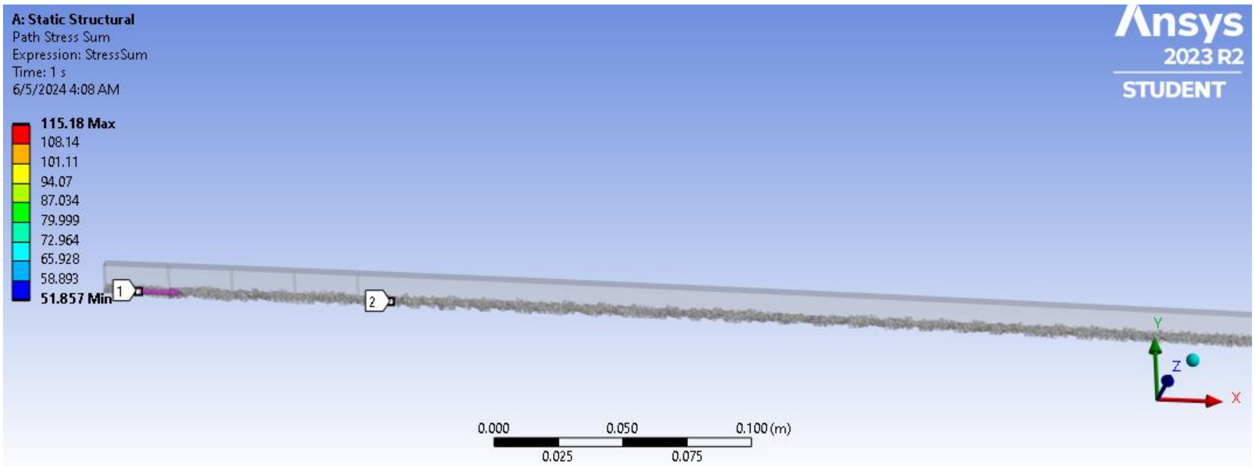

Figure 28 Path stress sum in ANSYS

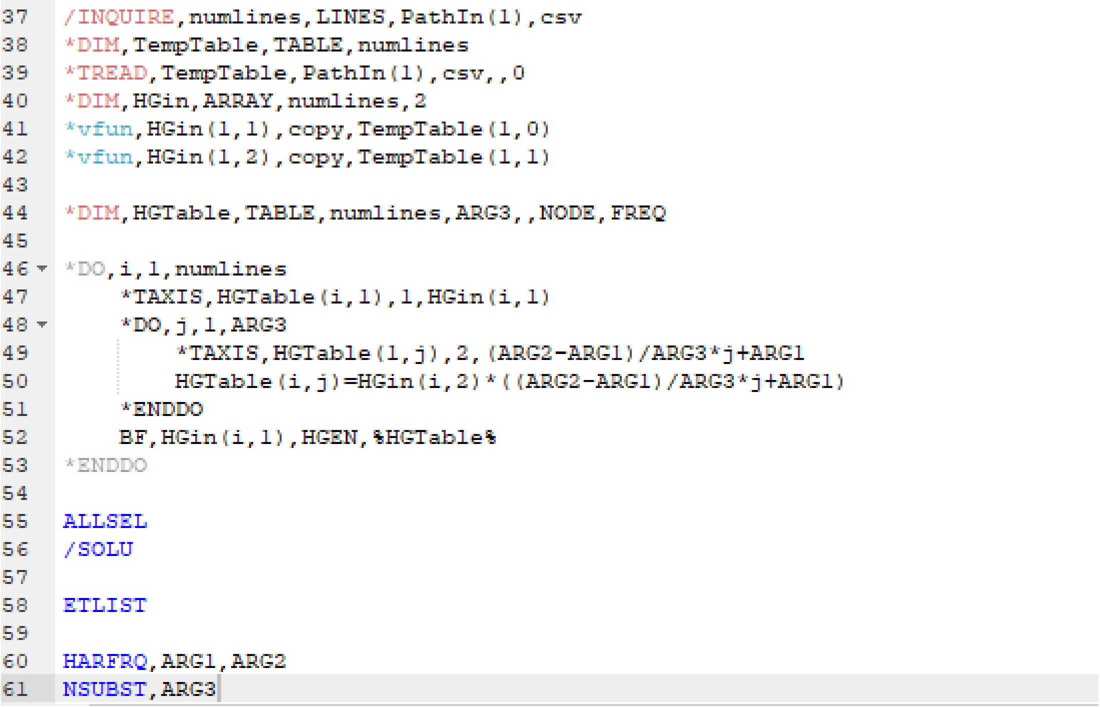

```
/INQUIRE,numlines,LINES,PathIn(1),csv
*DIM,TempTable,TABLE,numlines
*TREAD,TempTable,PathIn(1),csv,,0
*DIM,HGin,ARRAY,numlines,2
*vfun,HGin(1,1),copy,TempTable(1,0)
*vfun,HGin(1,2),copy,TempTable(1,1)

*DIM,HGTable,TABLE,numlines,ARG3,,NODE,FREQ

*DO,i,1,numlines
    *TAXIS,HGTable(i,1),1,HGin(i,1)
    *DO,j,1,ARG3
        *TAXIS,HGTable(1,j),2,(ARG2-ARG1)/ARG3*j+ARG1
        HGTable(i,j)=HGin(i,2)*((ARG2-ARG1)/ARG3*j+ARG1)
    *ENDDO
    BF,HGin(i,1),HGEN,%HGTable%
*ENDDO

ALLSEL
/SOLU

ETLIST

HARFRQ,ARG1,ARG2
NSUBST,ARG3
```

Figure 29 ANSYS code for thermal equation

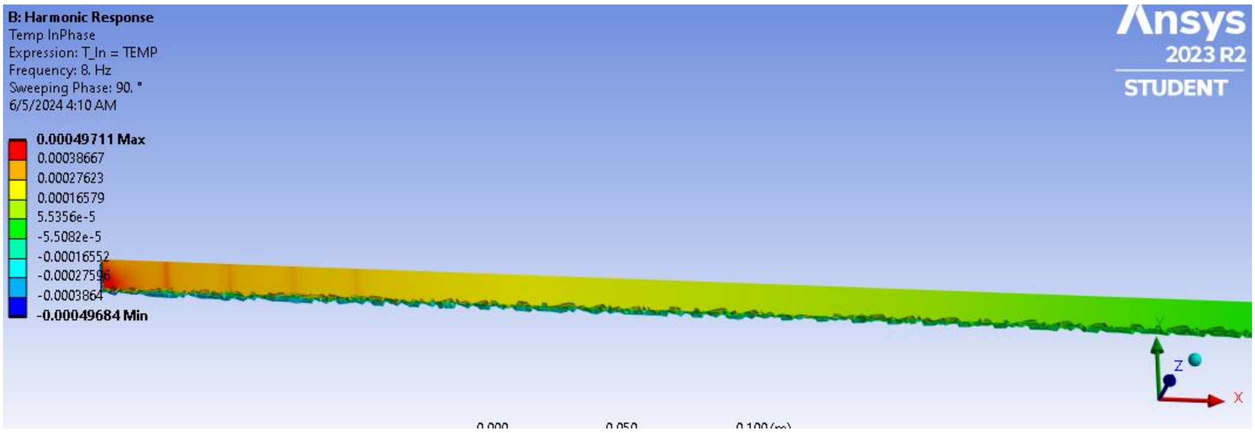

Figure 30 Temperature In phase in ANSYS

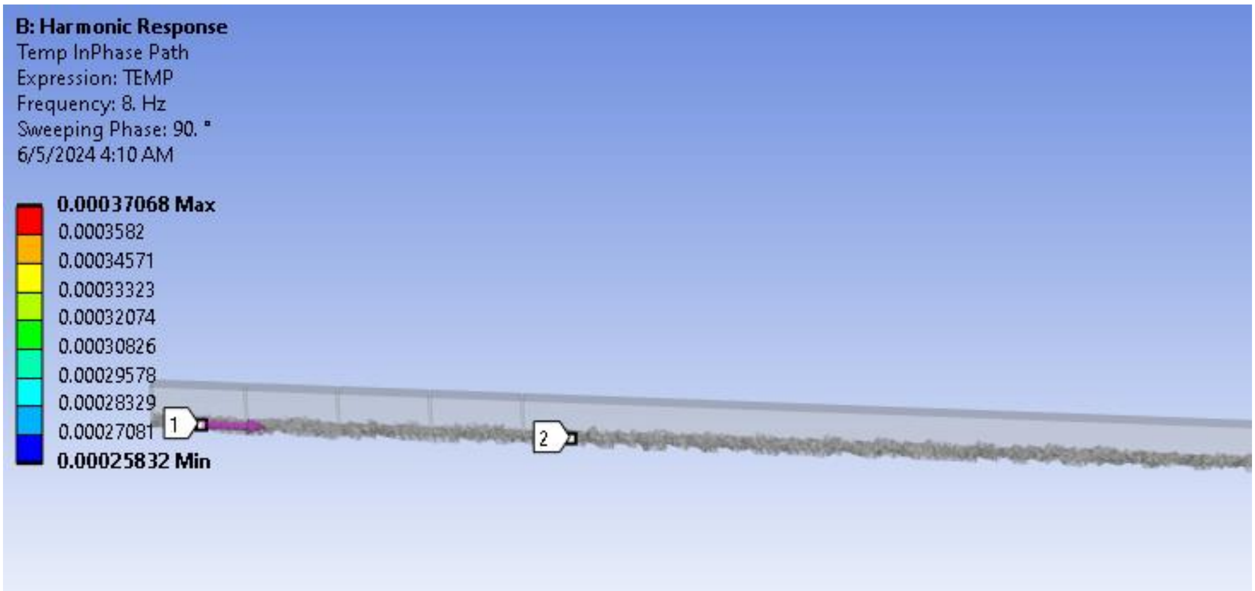

B: Harmonic Response
Temp InPhase Path
Expression: TEMP
Frequency: 8. Hz
Sweeping Phase: 90. °
6/5/2024 4:10 AM

Figure 31 Temperature in phase path

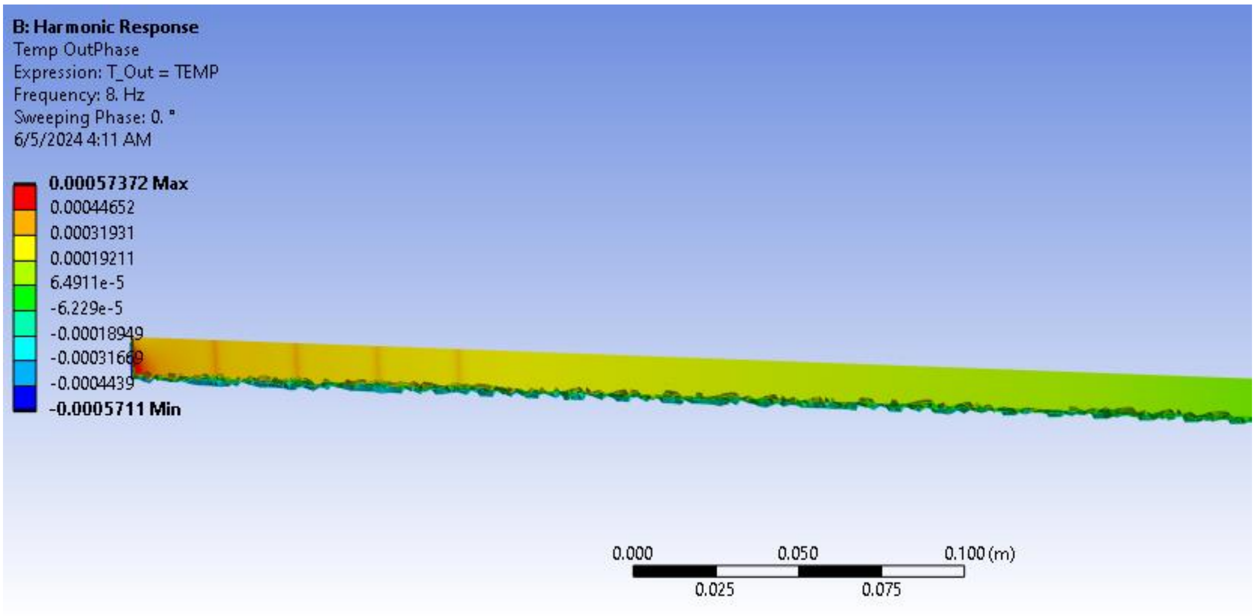

B: Harmonic Response
Temp OutPhase
Expression: T_Out = TEMP
Frequency: 8. Hz
Sweeping Phase: 0. °
6/5/2024 4:11 AM

Figure 32 Temperature out phase in ANSYS

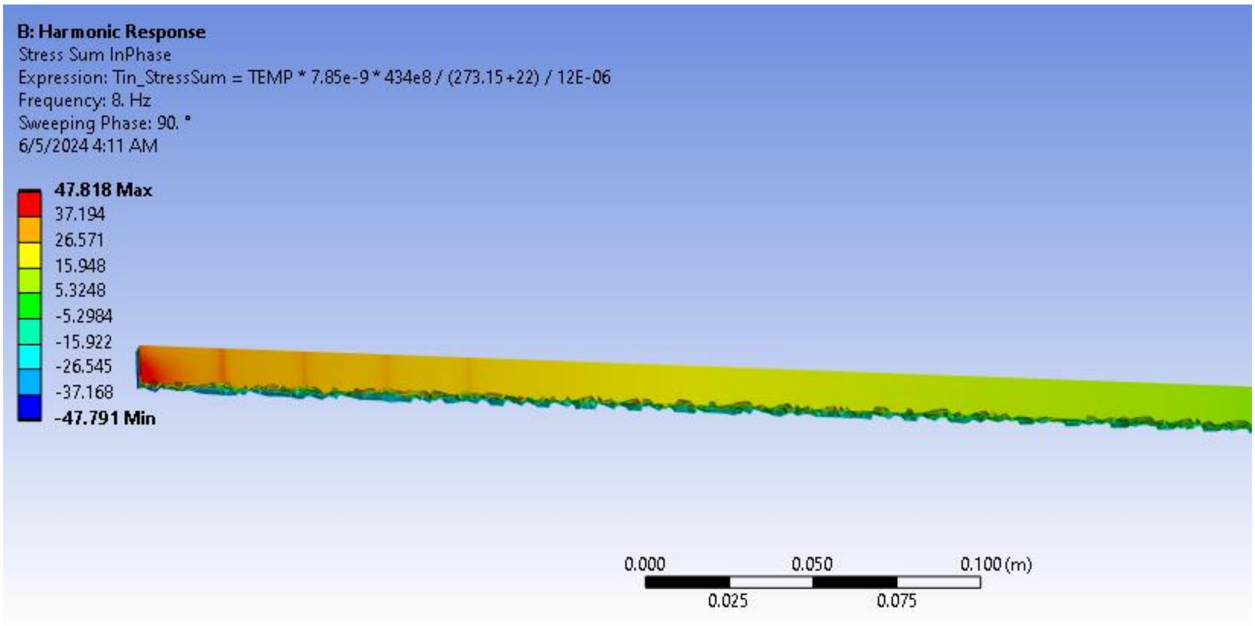

B: Harmonic Response
Stress Sum InPhase
Expression: Tin_StressSum = TEMP * 7.85e-9 * 434e8 / (273.15+22) / 12E-06
Frequency: 8. Hz
Sweeping Phase: 90. °
6/5/2024 4:11 AM

Figure 33 Stress sum in phase in ANSYS

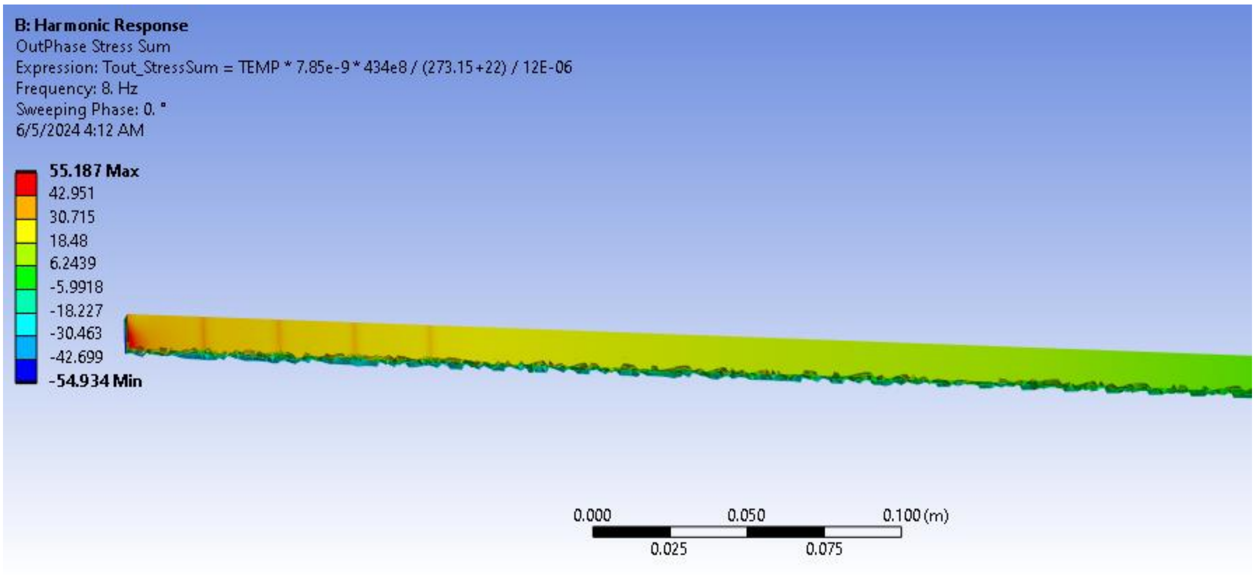

B: Harmonic Response
OutPhase Stress Sum
Expression: Tout_StressSum = TEMP * 7.85e-9 * 434e8 / (273.15+22) / 12E-06
Frequency: 8. Hz
Sweeping Phase: 0. °
6/5/2024 4:12 AM

Figure 34 Out phase stress sum in ANSYS

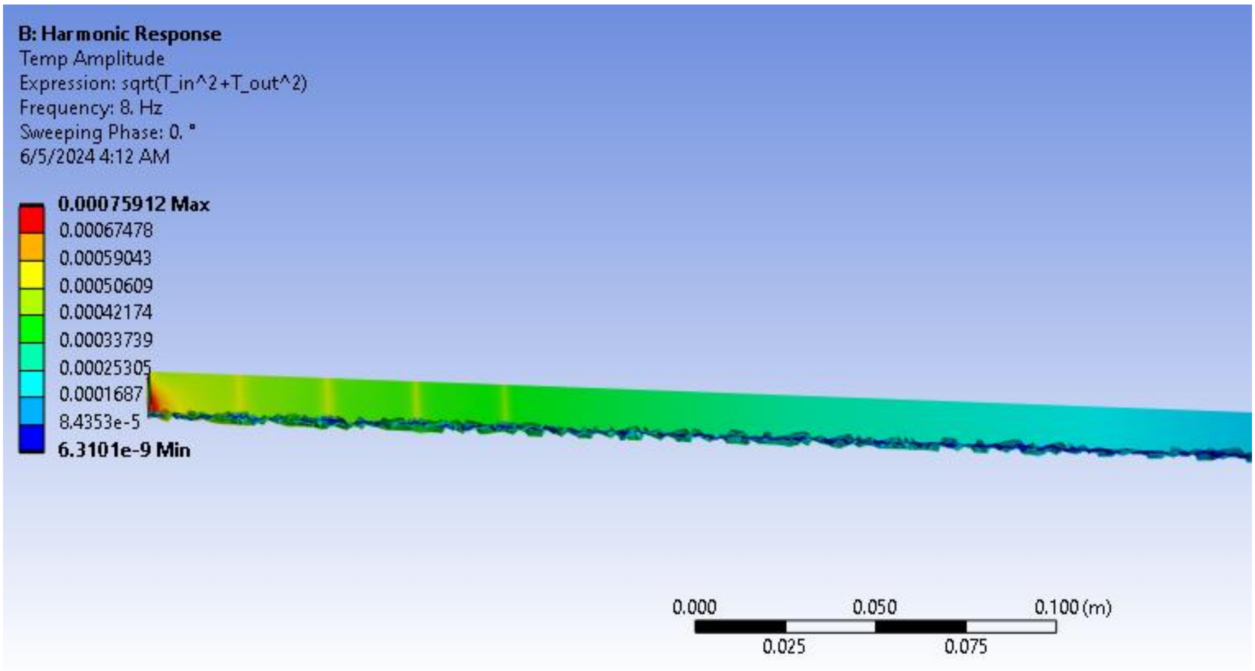

B: Harmonic Response
Temp Amplitude
Expression: sqrt(T_in^2+T_out^2)
Frequency: 8. Hz
Sweeping Phase: 0. °
6/5/2024 4:12 AM

Figure 35 Temperature amplitude in ANSYS

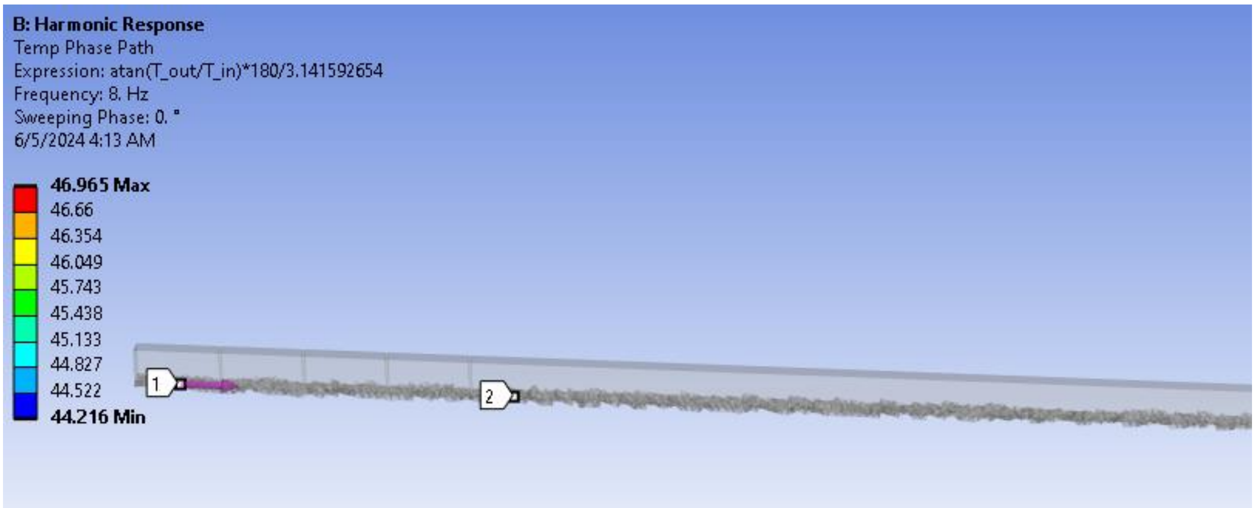

B: Harmonic Response
Temp Phase Path
Expression: atan(T_out/T_in)*180/3.141592654
Frequency: 8. Hz
Sweeping Phase: 0. °
6/5/2024 4:13 AM

Figure 36 Temperature Phase path in ANSYS

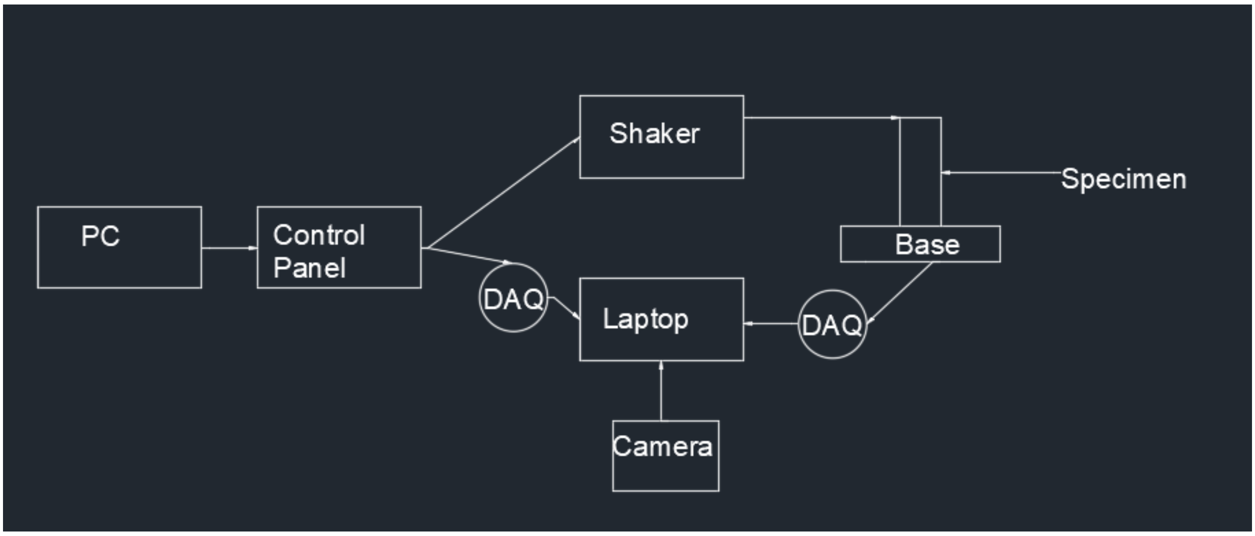

Figure 37 data Flow diagram from AutoCAD 2D

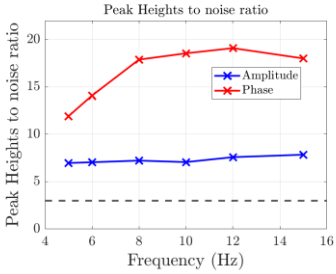

Figure 38 Peak heights to noise ratio from FEA

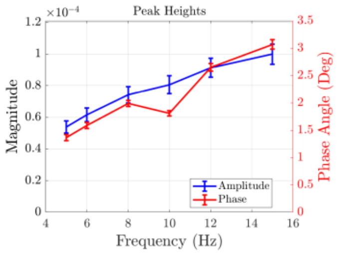

Figure 39 Peak height from FEA

Peaks height are increasing with increasing frequencies in FEA model. That is proved that higher frequency can show high peak.

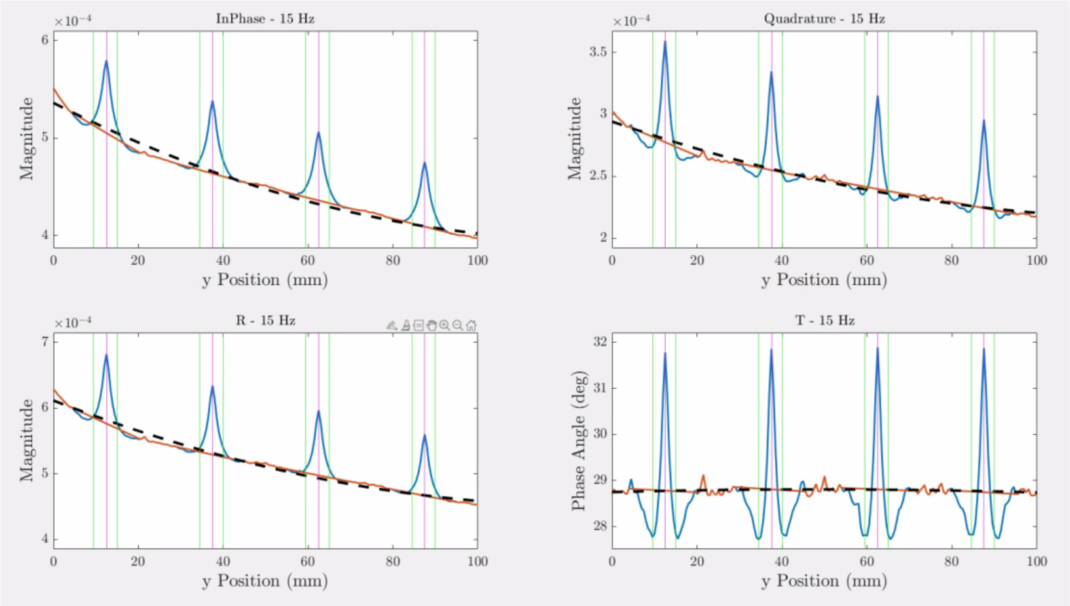

Figure 40 At 15 Hz frequency from FEA

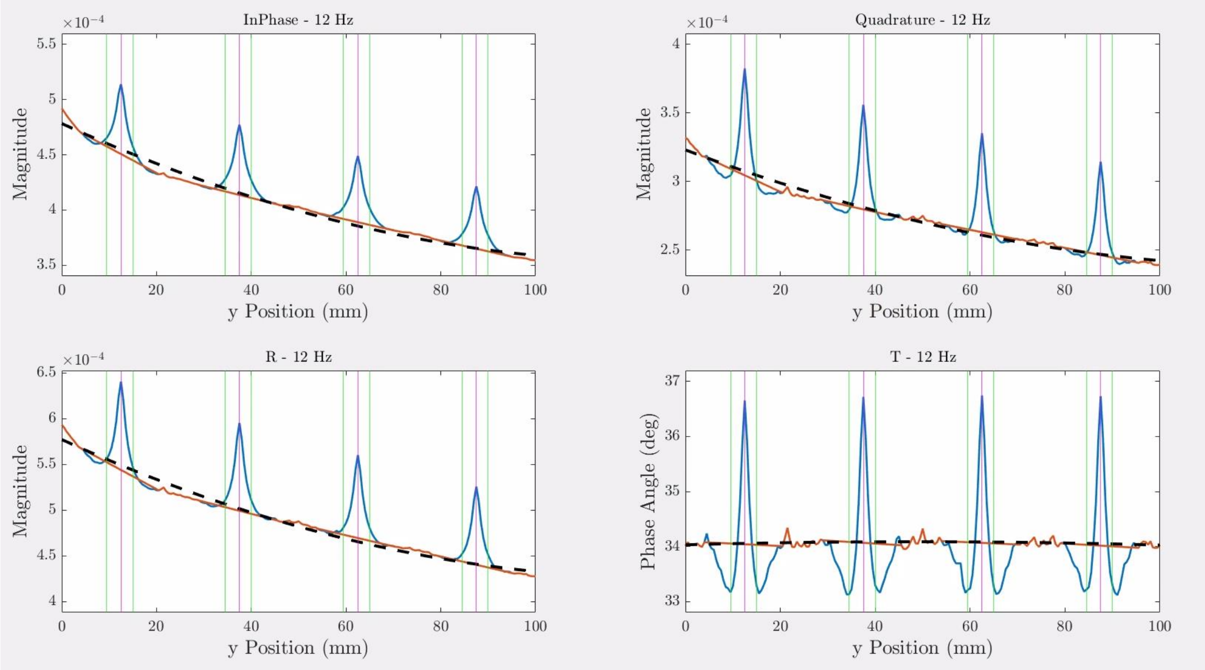

Figure 41 At 12 Hz frequency from FEA

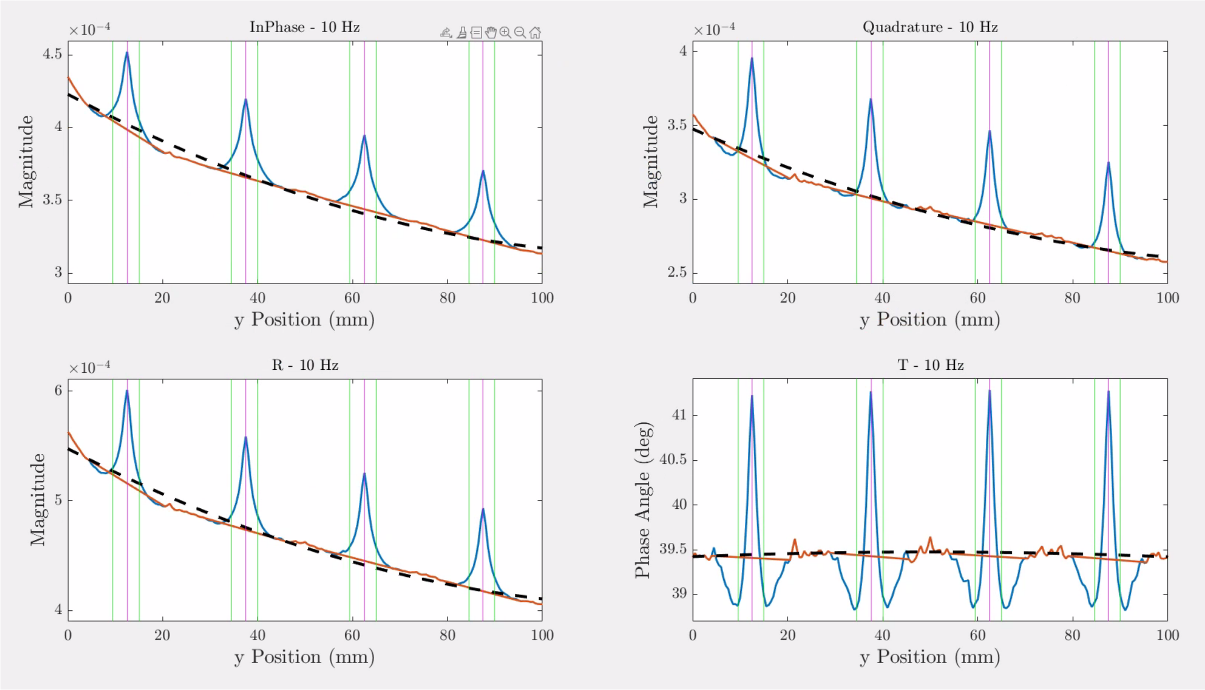

Figure 42 At 10 Hz frequency from FEA

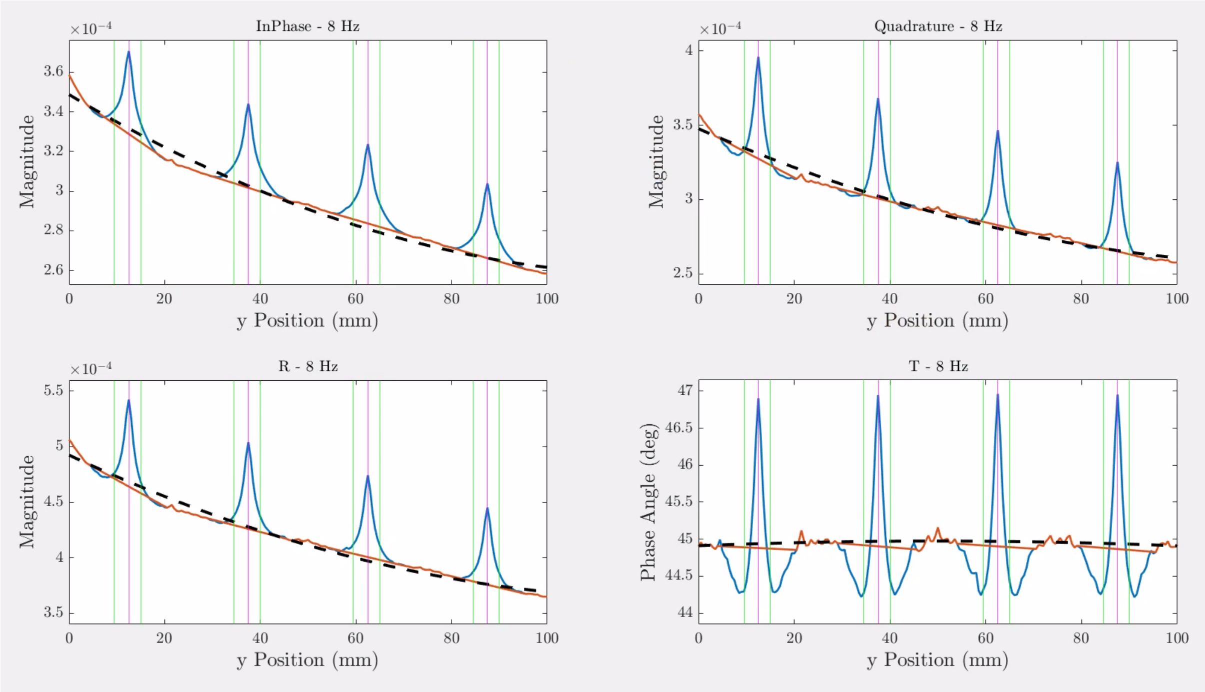

Figure 43 At 8 Hz frequency from FEA

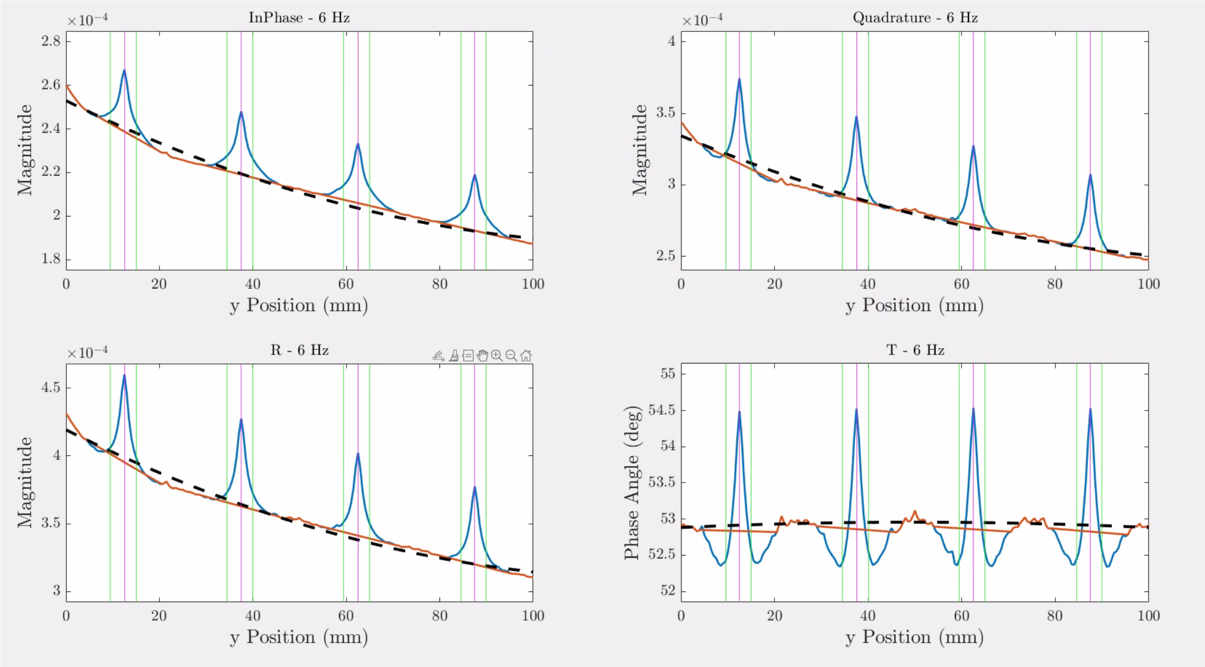

Figure 44 At 6 Hz frequency from FEA

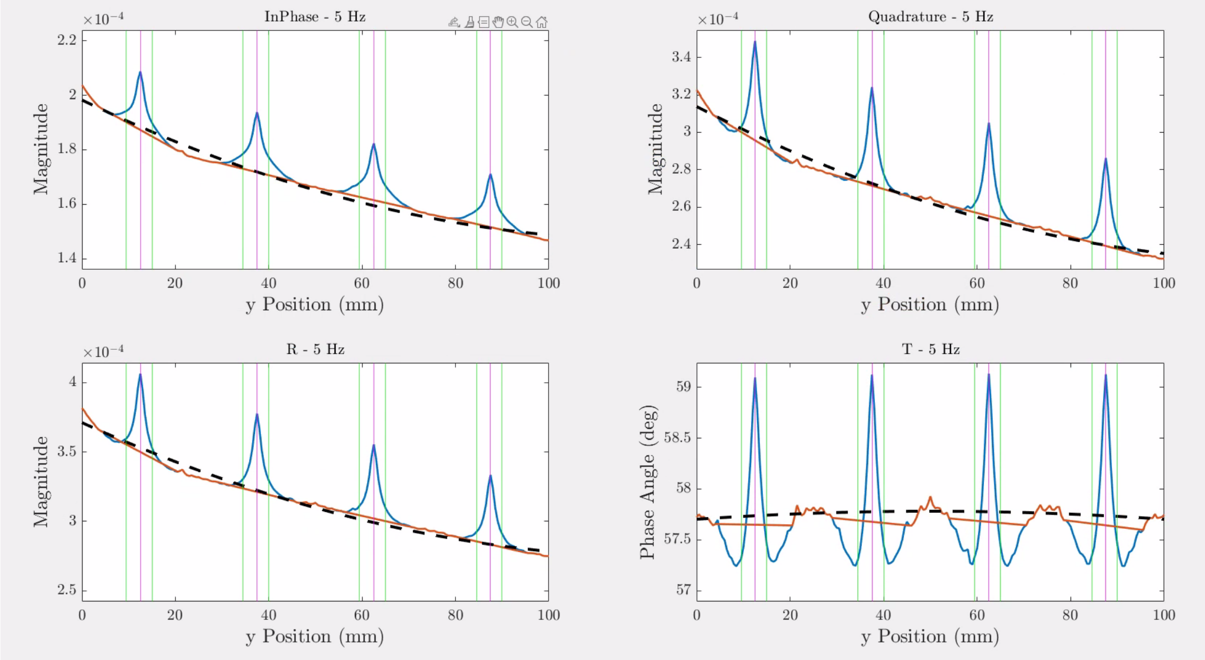

Figure 45 At 5 Hz frequency from FEA

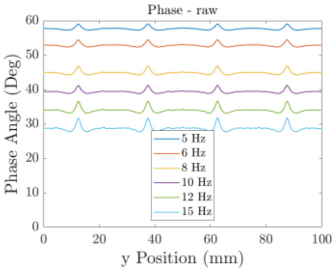

Figure 46 Frequency vs Phase angle from FEA

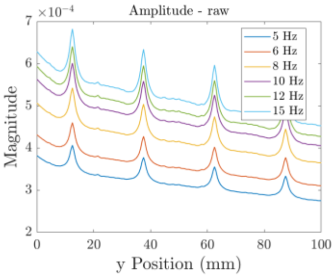

Figure 47 Frequency vs Magnitude from FEA